IEEE Open Access Journal of Power and Energy

Received 1 August 2023; revised 27 December 2023; accepted 27 January 2024.
Date of publication 30 January 2024; date of current version 20 February 2024.

Digital Object Identifier 10.1109/OAJPE.2024.3360091

Application of Extrapolation Capability of Vector Fitting for Out-of-Band Dominant Modal Synthesis of Voltage-Source Converters

WEIHUA ZHOU (Member, IEEE), AND JEF BEERTEN (Senior Member, IEEE)

Department of Electrical Engineering, KU Leuven, 3000 Leuven, Belgium
EnergyVille, 3600 Genk, Belgium
CORRESPONDING AUTHOR: W. ZHOU (weihua.zhou@ieee.org)

This work was supported by the Neptune Project through the Energy Transition Fund, FOD Economy, Belgium.

ABSTRACT Conventional state-space-based stability assessment method of voltage-source converters (VSCs) can be hindered by the black-box feature. Black box-based state-space model identification method using the terminal admittance/impedance frequency responses has thus been drawing increasing research attentions recently. However, the estimation of out-of-band modes commonly suffers from narrow bandwidth of frequency responses. This article presents, for the first time, the potential identification of several critical out-of-band modes of an artificially created rational function and a grid-connected VSC. This identification is achieved through their band-limited frequency responses using the vector fitting (VF) algorithm. On its basis, a sensitivity index of a partial fraction term is derived to explain the out-of-band modal identification behavior of the VF. The effects of the pole, residue, and fitting frequency interval width on the sensitivity index are further investigated and demonstrated. The numerical analysis shows that, with the help of the proposed sensitivity index, the extrapolation behavior of the VF can be explained, and several invisible out-of-band modes can further be identified or synthesized from a band-limited frequency response. This extrapolation feature may strengthen the curve fitting capability of the VF, i.e., compared to the VSC's band-limited frequency responses, more modal information can be obtained and further used for eigenvalue-based stability analysis.

INDEX TERMS Extrapolation, inverter, narrow-band frequency response, sensitivity index, stability, vector fitting.

NOMENCLATURE

AFR,IFR	Admittance and impedance frequency response.
BLFR	Band-limited frequency response.
EMT	Electromagnetic transient.
FDNE	Frequency-dependent network equivalent.
IBFR,OBFR	In-band and out-of-band frequency response.
MF,VF	Matrix fitting and vector fitting.
MIMO	Multiple-input-multiple-output.
PCC	Point-of-common-coupling.
SISO	Single-input-single-output.
SRF-PLL	Synchronous-reference-frame phase-locked loop.
SSM	State-space model.
VSC	Voltage-source converter.

I. INTRODUCTION

RECENTLY, conventional synchronous generators have been gradually replaced by inverter-based resources, e.g., wind and solar power [1]. The new paradigm leads to an increasing penetration of power electronic devices [2]. Different from the synchronous generators, various control loops of the inverters are commonly decoupled, and their bandwidths are commonly distributed at different time scales, which exposes the modern power systems to the risk of

wide-band low stability margin, resonance, or even instability under weak grid conditions [3].

The conventional eigenvalue-based stability analysis method, used to study these problems, builds the system state-space model (SSM) based on the detailed information on system structure and parameters [4], [5]. On its basis, the poorly-damped and unstable eigenvalues can be identified, and their participation factor analysis can further be performed in order to locate the root cause. Although mature and powerful, the state-space method can be hindered by the devices' black/gray-box feature [6], [7]. Since the admittance/impedance model is in essence the transfer function (matrix) reformulation of the SSM with appropriate input and output variables defined, the matrix fitting (MF) and vector fitting (VF) were recently applied as the inverse solving algorithms in order to identify the SSM from the admittance/impedance frequency responses (AFRs/IFRs) of the inverter-based power systems [8], [9], [10], [11]. With the help of the MF and VF, a virtual-eigenvalue-based participation factor analysis can for instance be performed on the black-box power systems.

The VF initially published in [12] aims to model the black-boxed power system apparatus, and has been conceived with mainly detailed time-domain electromagnetic transient (EMT)-type simulations in mind. As a routine, the VF aims to find a rational function approximation for a set of discrete frequency responses with the optimization objective being the minimized root-mean-square error over the fitting frequency range. It identifies the poles and residues by iteratively relocating an initial pole set which can be either real or complex conjugate pairs to better positions via a scaling function, each iterative step corresponding to the solution of simple well-conditioned linear systems. Thanks to its superior fitting performance, as demonstrated by the findings in [13] and [14], several engineering fields have attempted to improve the VF since its invention, among which power electronic domain [5], [6], [7], [8], [9], [15], [16], power system domain [17], [18], [19], [20], [21], [22], [23], [24], and electromagnetic compatibility domain [25], [26], [27], [28] are relatively active.

The VF fitting capability to cope with the scenarios where several frequency ranges coexist has been improved in [17] and [25] to relocate the poles, in [18], [19], [20], [21], and [16] to reduce the model order, and in [22], [23], and [24] to enhance the passivity which may be violated due to the out-of-band fitting errors encountered in the system identification procedure. In this article, band-limited frequency responses (BLFRs) are defined as the available AFR/IFR data covering a limited range of frequencies. In-band frequency responses (IBFRs) and out-of-band frequency responses (OBFRs) respectively refer to the frequency responses within this range, where AFRs/IFRs are available, and to those beyond this range that are not directly available. Specifically, the hard relocating process was presented in [25] to achieve better poles relocation able to converge more quickly and precisely, which was alternatively achieved in [17] by utilizing a novel mild summation requirement of the scaling function instead of the original stricter high-frequency asymptotic constraint. Consequently, [17] showed that the modes not situated in the frequency range where the initial poles were positioned were able to be identified based on a few times of poles relocation. Nevertheless, no modes of interest are beyond the available measurement frequency range.

In addition, the overall frequency band of interest was split in [18], [19], [20], [21], and [16] into a few narrow intervals, and the VF was used to generate an order-reduced model for each small frequency range. However, the effects of these generated order-reduced models on the frequency responses within adjacent intervals were ignored in [18] and [16]. On the contrary, the fitting inaccuracy of the order-reduced model generated from the low-frequency band in the high-frequency band and the fitting inaccuracy of the order-reduced model generated from the high-frequency band at about DC point below 1 Hz were eliminated in [19], [20], and [21], respectively. Nevertheless, the out-of-band fitting accuracy improvement in [19], [20], and [21] supposed that OBFRs were already available. Therefore, it is necessary to estimate the OBFRs using solely the IBFRs.

Furthermore, several out-of-band passivity enforcement strategies were presented in [22], [23], and [24] by disturbing the residues, poles, or residue matrices' eigenvalues of the generated rational model, due to the possible passivity violation induced by the VF. Thanks to these research efforts, the current version of the VF can be configured flexibly to guarantee the passivity of the fitted rational approximations and stability of the EMT simulation. However, the accurate reproduction of the OBFRs may not be achieved by these out-of-band passivity enforcement strategies.

Attempts to extrapolate the BLFRs using solely the IBFRs were performed in [26], [27], [28], [29], [30], and [31]. For example, on one hand, to guarantee the causality of the impulse responses of the low-frequency IBFRs of the S-parameters, the Hilbert transformation was employed in [26] and [27] to extrapolate the IBFRs to generate the OBFRs in the high-frequency band. On the other hand, to guarantee the delay causality of the time responses of the middle-frequency IBFRs of the S-parameters, the Kramers-Kronig relation was employed in [28] to extrapolate the IBFRs to generate the OBFRs in low-and high-frequency bands simultaneously. However, like the out-of-band passivity enhancement strategies developed in [22], [23], and [24], the out-of-band modal identification may still not be ensured by these causality enforcement strategies in [26], [27], and [28]. The out-of-band modes were proved in [12] to make little effect on the in-band fitting precision, whereas no out-of-band modal identification were performed. Differently, higher order of the denominator or numerator was assigned in [29], [30], and [31] to eliminate the in-band fitting inaccuracy induced by the residual influences of the partial fraction terms located within

the out-of-band frequency band. As a result, if one more order is assigned for the denominator, an out-of-band partial fraction term is identified with high precision. However, the explanation of the extrapolation behavior was not provided.

Due to the industry secrecy and intellectual property protection, the discrete AFRs of the voltage-source converters (VSCs) tend to be delivered in the lookup table form as shown in [8], and [6]. However, the frequency range of the provided lookup tables may be narrow, which probably does not satisfy the stability analysis requirement in wide frequency range. Alternatively, if the black-box models of the VSCs are available, the frequency sweeping either using the commercial software (e.g., PSCAD/EMTDC and Matlab/Simulink) as shown in [9] and [32] or in the laboratory as shown in [33] and [34] can be performed. However, whether the measurement results within different narrow frequency ranges are accurate or not is uncertain. To cope with these practical issues, this article, based on the authors' previous work in [35] and [36] which focused on the selective identifications of dominant poles and residues of the artificially created rational functions with the help of the VF/MF, intends to apply the frequency-domain extrapolation capability of the VF/MF for black box-based stability assessment of the VSCs. Specifically, if the AFRs of the VSCs in the form of lookup table have narrow frequency range, the VF/MF can be employed to predict the out-of-band AFRs by extrapolating the available BLFRs. In addition, if the wide-band AFRs of the VSCs are obtained by performing the frequency sweeping on the simulation models or in the lab, the VF/MF can be employed to cross check the accuracy of the AFRs within different narrow frequency ranges.

The main contributions of this article can be summarized as follows.

- A sensitivity index of each partial fraction term is developed to quantify the effect of the inaccurate identification of the in-band and out-of-band partial fraction terms on the in-band fitting inaccuracy.
- The internal mechanism behind the selective in-band modal identification of the under-fitted models and selective out-of-band modal identification of the over-fitted models are revealed.
- The dominant out-of-band modes of grid-connected VSCs under current and voltage control modes are synthesized from the over-fitted models using the proposed sensitivity index.

The rest of this article is organized as follows. The basic principle of the VF, and the extrapolation behavior for a set of single-input-single-output (SISO) BLFRs of an artificially created rational function and for a set of multiple-input-multiple-output (MIMO) BLFRs of a VSC are shown in Section II. In Section III, the sensitivity index of the partial fraction term is derived to explore the internal mechanism of the extrapolation capability of VF. The feasibility of the proposed sensitivity index is verified in Section IV using the artificially created rational function. In Section V, the proposed sensitivity index concept is further verified using the current- and voltage-controlled VSCs to identify the dominant out-of-band modes. Finally, the conclusions are drawn in Section VI.

II. EXTRAPOLATION BEHAVIOR FOR THE BLFRs

A. BASIC PRINCIPLE OF THE VF

The VF can generate a rational function approximation $f(s)$ for K discrete frequency samples $\{H(j\omega_k)|k=1,2,\ldots,K\}$, i.e., [12]

$$H(s)|_{s=j\omega_k} \approx f(s)|_{s=j\omega_k} = \sum_{i=1}^{N} \frac{r_i}{s-p_i} + d, \tag{1}$$

where N is the fitting order of $f(s)$. In addition, the poles $\{p_i|i=1,2,\ldots,N\}$ and residues $\{r_i|i=1,2,\ldots,N\}$ are either real values or complex conjugate pairs. d is the direct term which can be either real or optional. The VF routine consists of three stages, i.e., poles initialization, poles identification, and residues identification.

Poles Identification: The key to the poles relocation is the design of a scaling function $\sigma^t(s)$ as

$$\sigma^t(s) = \frac{\prod_{i=1}^{N}\left(s-\widehat{z_i^t}\right)}{\prod_{i=1}^{N}\left(s-q_i^t\right)} = \sum_{i=1}^{N}\frac{\widehat{k_i^t}}{s-q_i^t} + 1, \tag{2}$$

where t denotes the iteration number. $\{q_i^t|i=1,2,\ldots,N\}$ is the tth iterative estimation for $\{p_i|i=1,2,\ldots,N\}$. $\{\widehat{z_i^t}|i=1,2,\ldots,N\}$ and $\{\widehat{k_i^t}|i=1,2,\ldots,N\}$ are the zeros and residues collection, respectively, of $\sigma^t(s)$. The poles in the next iteration are replaced by the zeros in current iteration, i.e., $\{q_i^{t+1}\} = \{\widehat{z_i^t}\}$. In each iteration, $\sigma^t(s)H(s)$ is approximated by another rational function $\left(\sigma^t H\right)_{fit}(s)$ using the same set of poles of $\sigma^t(s)$, i.e.,

$$\left(\sigma^t H\right)_{fit}(s) = \sum_{i=1}^{N}\frac{k_i^t}{s-q_i^t} + d, \tag{3}$$

where $\{k_i^t|i=1,2,\ldots,N\}$ is the residues collection of $\left(\sigma^t H\right)_{fit}(s)$. Based on (2) and (3), at a specific frequency point $s_k = j\omega_k$ ($k \in [1,K]$), one can have

$$\sum_{i=1}^{N}\frac{k_i^t}{j\omega_k - q_i^t} + d = \left(\sum_{i=1}^{N}\frac{\widehat{k_i^t}}{j\omega_k - q_i^t} + 1\right)H(j\omega_k), \tag{4}$$

which can be reformulated as a least-square problem as

$$A_k \overrightarrow{X} = b_k, \tag{5}$$

where

$$\begin{aligned} A_k &= \left[\frac{1}{j\omega_k - q_1^t}, \ldots, \frac{1}{j\omega_k - q_N^t}, 1, \frac{-H(j\omega_k)}{j\omega_k - q_1^t}, \ldots, \frac{-H(j\omega_k)}{j\omega_k - q_N^t}\right], \\ \overrightarrow{X} &= \left[k_1^t, \ldots, k_N^t, d, \widehat{k_1^t}, \ldots, \widehat{k_N^t}\right]^{\mathrm{T}}, \qquad b_k = H(j\omega_k). \end{aligned} \tag{6}$$

Based on the obtained residues (i.e., $\widehat{k_1^t}$, $\widehat{k_2^t}$, …, and $\widehat{k_N^t}$), the zeros (i.e., $\widehat{z_1^t}$, $\widehat{z_2^t}$, …, and $\widehat{z_N^t}$) can further be calculated using (2).

If the poles relocation converges, i.e., $\{q_i^{t+1}|i = 1, 2, \ldots, N\} = \{q_i^t|i = 1, 2, \ldots, N\}$, one can have from (2) and (4) that

$$p_i = q_i^t = \widehat{z_i^t}, \qquad \widehat{k_i^t} = 0, \qquad r_i = k_i^t, \tag{7}$$

for $i = 1, 2, \ldots, N$, which indicates that the poles identification of $f(s)$ becomes the zeros identification of $\sigma^t(s)$.

Residues Identification: Although (6) and (7) already provide the solutions of the asymptotic term d and the residues $\{r_i|i = 1, 2, \ldots, N\}$, respectively, the determined poles $\{p_i|i = 1, 2, \ldots, N\}$ in (7) are substituted into (1) to calculate more accurately d and $\{r_i|i = 1, 2, \ldots, N\}$ through formulating another least-square problem.

The under-fitting and over-fitting behaviors of VF are explored in this section. Under-fitting is characterized by a fitting order that is lower than the system's actual order, and over-fitting occurs when the fitting order is higher than the actual system order.

B. FIRST LOOK AT THE EXTRAPOLATION BEHAVIOR FOR THE BLFRs

1) EXTRAPOLATION FOR AN ARTIFICIALLY CREATED RATIONAL FUNCTION

Table 1 presents an artificially created rational function $H(s)$ in the form of (1) with $N = 44$ and $d = 0.0032$. This investigated rational function does not have real zeros and real poles, since out-of-band modal identification is the focus. The imaginary parts of the poles of the 22 pairs of partial fraction terms are distributed below 10 kHz. In addition, the differences among the residues and the real parts of the poles of the 22 pairs of partial fraction terms are designed as small enough to test if the VF can identify these discrepancies.

TABLE 1. Poles and Residues of the Artificially Created Rational Function $H(s)$ in the Form of (1).

(p_i, r_i)	(p_i, r_i)
#1: (-10±j2764.60, 20±j80)	#2: (-11±j5780.53, 21±j81)
#3: (-12±j8356.64, 22±j82)	#4: (-13±j11561.06, 23±j83)
#5: (-14±j13948.67, 24±j84)	#6: (-15±j17027.43, 25±j85)
#7: (-16±j19980.53, 26±j86)	#8: (-17±j22493.80, 27±j87)
#9: (-18±j25258.40, 28±j88)	#10: (-19±j28085.84, 29±j89)
#11: (-20±j30976.10, 30±j90)	#12: (-21±j34054.86, 31±j91)
#13: (-22±j36819.47, 32±j92)	#14: (-23±j39521.24, 33±j93)
#15: (-24±j42474.33, 34±j94)	#16: (-25±j45176.10, 35±j95)
#17: (-26±j48003.54, 36±j96)	#18: (-27±j51082.30, 37±j97)
#19: (-28±j53784.07, 38±j98)	#20: (-29±j56485.84, 39±j99)
#21: (-30±j59438.93, 40±j100)	#22: (-31±j62140.70, 41±j101)

In order to observe the under-fitting behavior of the VF, Fig. 1(a) shows the Bode diagrams of the under-fitting results for the 4000 uniformly-spread frequency points of $H(s)$ between 3001 and 7000 Hz using initial poles uniformly located within [3001, 7000] Hz and different fitting orders, i.e., 2nd, 4th, and 6th. The poles of the fitted 2nd-order rational function $f_{2nd}(s)$ are $-1446.4 \pm j2\pi 7120.91$, the imaginary part of which is close to that of the #16 amplitude peak. In addition, the poles of the fitted 4th-order rational function $f_{4th}(s)$ are $-734.58 \pm j2\pi 2980.4$ and $-1684.5 \pm j2\pi 7132.4$, the imaginary parts of which are close to those of the #7 and #16 amplitude peaks. Furthermore, the poles of the fitted 6th-order rational function $f_{6th}(s)$ are $-714.53 \pm j2\pi 2996.3$, $-355.15 \pm j2\pi 4942.8$, and $-1373.9 \pm j2\pi 7065.6$, the imaginary parts of which are close to those of the #7, #11, and #16 amplitude peaks. These fitting results indicate that the VF preferentially captures the magnitude peaks that are closest to the boundaries of the fitting frequency range, and then captures the in-band amplitude peaks.

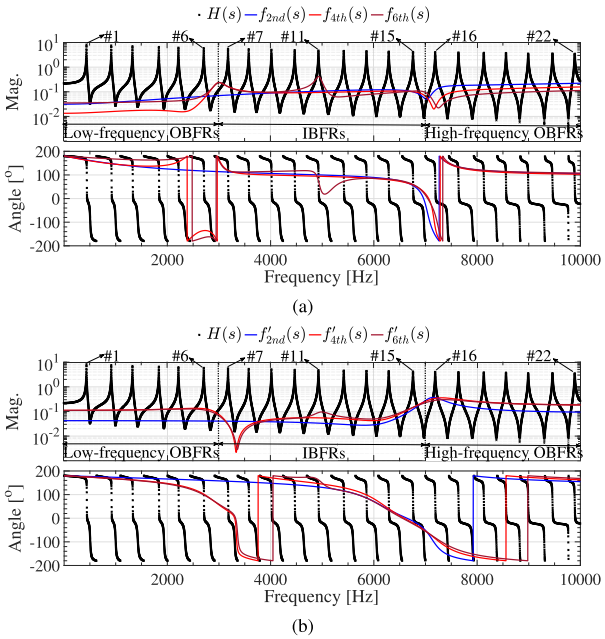

FIGURE 1. Bode diagrams of the under-fitting results for the BLFRs of $H(s)$ based on (a) 4000 and (b) 40 frequency sampling points within [3001, 7000] Hz.

To check the VF's fitting performance when fewer frequency sampling points are available, Fig. 1(b) shows the Bode diagrams of the under-fitting results when the number of the frequency sampling points is decreased from 4000 as shown in Fig. 1(a) to 40. The poles of the fitted 2nd-order rational function $f'_{2nd}(s)$ are $-1187.5 \pm j2\pi 7124.5$, the imaginary part of which is close to that of the #16 amplitude peak. In addition, the poles of the fitted 4th-order rational function $f'_{4th}(s)$ are $-2384.1 \pm j2\pi 2915.8$ and $-2372.5 \pm j2\pi 7182.8$, the imaginary parts of which are close to those of the #7 and #16 amplitude peaks. Furthermore, the poles of the fitted 6th-order rational function $f'_{6th}(s)$ are $-2848.2 \pm j2\pi 2906.4$, $-1003.5 \pm j2\pi 4975.3$, and $-3034.1 \pm j2\pi 7174.2$, the imaginary parts of which are close to those of the #7, #11, and #16 amplitude peaks. It can be seen that these fitting behaviors are similar to those shown in Fig. 1(a).

In order to observe the over-fitting behaviors of the VF, Fig. 2(a) shows the Bode diagrams of the extrapolation results for the 6000 uniformly-spread frequency points of $H(s)$ between 2001 and 8000 Hz using initial poles evenly situated within [2001, 8000] Hz and different fitting orders, i.e., 32th, 38th, 44th, and 50th. Fig. 2(a) shows that the IBFRs can be identified by all of the four fitted rational functions with high precision. In addition, the fitted 32th-order rational function $f_{32th}(s)$ has two amplitude peaks that are located outside the fitting frequency interval and poorly capture the original two amplitude peaks, i.e., the #4 and #18 magnitude peaks. Differently, the fitted 38th-order rational function $f_{38th}(s)$ can accurately capture the two out-of-band amplitude peaks that are closest to the boundaries of the fitting frequency interval. Furthermore, the fitted 44th-order rational function $f_{44th}(s)$ and 50th-order rational function $f_{50th}(s)$ can capture all the nine out-of-band amplitude peaks, i.e., the #1-#4 and #18-#22 magnitude peaks. These fitting results indicate that the VF preferentially captures the amplitude peaks that are closest to the boundaries of the fitting frequency interval, and the extrapolation capability of the VF can be improved if the fitting order is increased. These observations are confirmed by the poles distribution in Fig. 2(b) and residues distribution in Fig. 2(c), where $P(\cdot)$ denotes the poles operator and $R(\cdot)$ denotes the residues operator. Note that only positive imaginary parts of the poles and residues are plotted for simplicity. Compared to the fitted 44th-order rational function $f_{44th}(s)$, it can be seen from Fig. 2(c) that the fitted 50th-order rational function $f_{50th}(s)$ has additional six residues located at the origin, which explains why $f_{44th}(s)$ and $f_{50th}(s)$ share the same frequency responses as shown in Fig. 2(a).

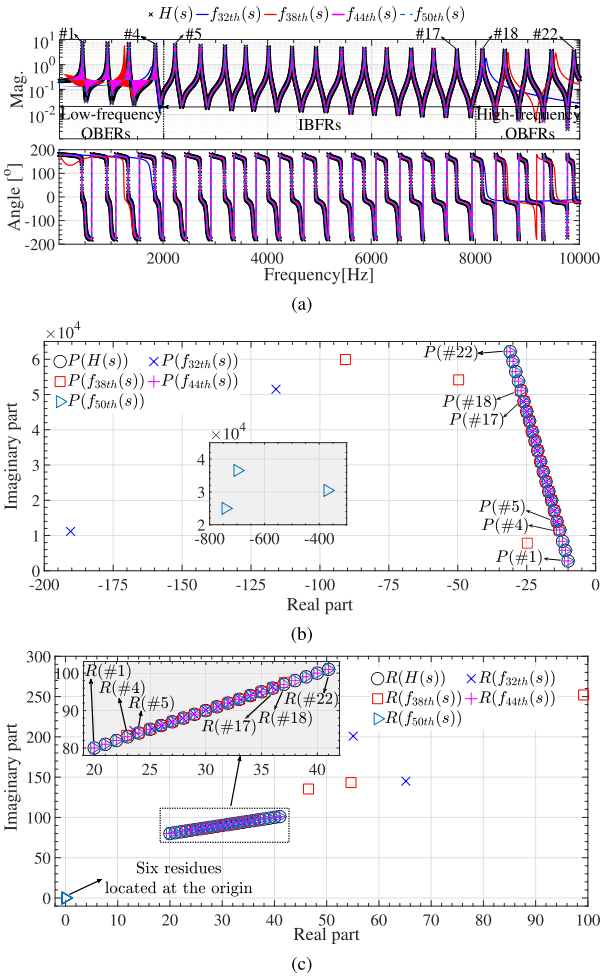

FIGURE 2. Over-fitting results for the BLFRs of $H(s)$ within [2001, 8000] Hz. (a) Bode plots, (b) poles distribution, and (c) residues distribution.

2) EXTRAPOLATION FOR A GRID-CONNECTED VSC

Given that both the artificially created rational function $H(s)$ and its various fitted approximations (such as $f_{2nd}(s)$, $f_{4th}(s)$, etc.) in Section II-B.1 follow the form of (1), it is expected that satisfactory fitting results could be achieved for $H(s)$ with a high enough fitting order. However, this approach, particularly the linear distribution of poles in the artificially created rational function as per Table 1, may be an oversimplification when considering the complexities of real-world systems. In real-world scenarios, especially in systems like grid-connected VSCs, poles are often distributed logarithmically rather than linearly. Recognizing this discrepancy, the latter part of this section transitions to explore the application of the VF method to non-linear VSCs characterized by logarithmically distributed poles.

Fig. 3 shows the single-line diagram of the grid-following VSC system under study. The high-frequency switching harmonics are filtered by the LCL filter composed of converter-side inductance L_{f1} with parasitic resistance R_{f1}, grid-side inductance L_{f2} with parasitic resistance R_{f2}, and capacitance C_f. The current controller $G_i(s)$ is based on the standard PI controller. The superscript c denotes that the variables are represented in the controller dq reference frame. The synchronous-reference-frame phase-locked loop (SRF-PLL) is used to align the phase angle of the injected current with that of point-of-common-coupling (PCC) voltage. The digital and computational time delay is denoted as $T_d = 1.5/f_s$, where f_s is the sampling frequency. The circuit and controller parameters are listed in Table 9 of Appendix. Since the sampling frequency f_s is chosen as 5 kHz, the Nyquist frequency which is equal to half of the sampling frequency (i.e., 2.5 kHz) is selected as the high-frequency limit for the VSC under analysis.

The average model of the VSC is employed in this article without considering the switching phenomenon effect. Based on the small-signal linearization, the dq-domain admittance model of the VSC (i.e., Y_{vsc}) can be derived. Different from the artificially created rational function $H(s)$ listed in Table 1, the Y_{vsc} is in the form of the polynomial transfer function, which hinders the explicit separation of the in-band and out-of-band eigenvalues pairs. To this end, the partial fraction expansion is employed to split Y_{vsc} into eight pairs of partial fraction terms (i.e., $A_{1,2}$, $B_{1,2}$,..., and $H_{1,2}$), of which the poles and resides are listed in Table 2.

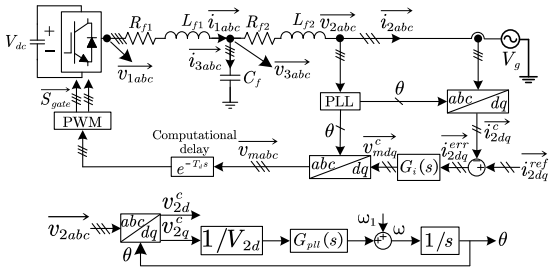

FIGURE 3. **The studied grid-connected VSC system.**

TABLE 2. **Poles and Residues of the *DQ*-Domain Admittance Transfer Function Matrix Y_{VSC} of the VSC.**

$P(Y_{vsc})$	$\begin{bmatrix} R_{dd}(Y_{vsc}) & R_{dq}(Y_{vsc}) \\ R_{qd}(Y_{vsc}) & R_{qq}(Y_{vsc}) \end{bmatrix}$
$P(A_{1,2})$: $(-167.80 \pm j421.75)$	$\begin{bmatrix} R_{dd}(A_{1,2}) & R_{dq}(A_{1,2}) \\ R_{qd}(A_{1,2}) & R_{qq}(A_{1,2}) \end{bmatrix}$: $\begin{bmatrix} 913.15 \pm j106.26 & 125.95 \mp j918.23 \\ -106.26 \pm j913.15 & 918.23 \pm j125.95 \end{bmatrix}$
$P(B_{1,2})$: $(-34.9894 \pm j87.0246)$	$\begin{bmatrix} R_{dd}(B_{1,2}) & R_{dq}(B_{1,2}) \\ R_{qd}(B_{1,2}) & R_{qq}(B_{1,2}) \end{bmatrix}$: $\begin{bmatrix} 152.05 \pm j113.30 & -132.98 \pm j145.81 \\ 113.30 \mp j152.05 & 145.81 \pm j132.98 \end{bmatrix}$
$P(C_{1,2})$: $(-5.0000 \pm j5.0000)$	$\begin{bmatrix} R_{dd}(C_{1,2}) & R_{dq}(C_{1,2}) \\ R_{qd}(C_{1,2}) & R_{qq}(C_{1,2}) \end{bmatrix}$: $\begin{bmatrix} 0 \pm 0 & 0.0045 \pm j0.1027 \\ 0 \pm 0 & -7.4427 \mp j1.3045 \end{bmatrix}$
$P(D_{1,2})$: $(-88.969 \pm j12388)$	$\begin{bmatrix} R_{dd}(D_{1,2}) & R_{dq}(D_{1,2}) \\ R_{qd}(D_{1,2}) & R_{qq}(D_{1,2}) \end{bmatrix}$: $\begin{bmatrix} 514.13 \mp j4.2180 & 3.8030 \pm j514.14 \\ -4.2180 \mp j514.13 & 514.14 \mp j3.8030 \end{bmatrix}$
$P(E_{1,2})$: $(-78.193 \pm j13030)$	$\begin{bmatrix} R_{dd}(E_{1,2}) & R_{dq}(E_{1,2}) \\ R_{qd}(E_{1,2}) & R_{qq}(E_{1,2}) \end{bmatrix}$: $\begin{bmatrix} 512.81 \mp j6.3384 & -5.9449 \mp j512.82 \\ 6.3384 \pm j512.81 & 512.82 \mp j5.9449 \end{bmatrix}$
$P(F_{1,2})$: $(-12587 \pm j11307)$	$\begin{bmatrix} R_{dd}(F_{1,2}) & R_{dq}(F_{1,2}) \\ R_{qd}(F_{1,2}) & R_{qq}(F_{1,2}) \end{bmatrix}$: $\begin{bmatrix} 13.3944 \pm j54.6712 & -54.7005 \pm j13.3787 \\ 54.6712 \mp j13.3944 & 13.3787 \pm j54.7005 \end{bmatrix}$
$P(G_{1,2})$: $(-12636 \pm j11327)$	$\begin{bmatrix} R_{dd}(G_{1,2}) & R_{dq}(G_{1,2}) \\ R_{qd}(G_{1,2}) & R_{qq}(G_{1,2}) \end{bmatrix}$: $\begin{bmatrix} 20.9212 \pm j54.3912 & 54.4233 \mp j20.9089 \\ -54.3912 \pm j20.9212 & 20.9089 \pm j54.4233 \end{bmatrix}$
$P(H_{1,2})$: $(-14415 \pm j54.207)$	$\begin{bmatrix} R_{dd}(H_{1,2}) & R_{dq}(H_{1,2}) \\ R_{qd}(H_{1,2}) & R_{qq}(H_{1,2}) \end{bmatrix}$: $\begin{bmatrix} -126.45 \mp j9.4379 & 9.4448 \mp j126.54 \\ -9.4379 \pm j126.45 & -126.54 \mp j9.4448 \end{bmatrix}$

Note: $P(\cdot)$ denotes the poles operator. $R_{dd}(\cdot)$, $R_{dq}(\cdot)$, $R_{qd}(\cdot)$, and $R_{qq}(\cdot)$ denote the *dd*-, *dq*-, *qd*-, and *qq*-axis residues operators, respectively.

In order to observe the under-fitting behavior of the MF, Fig. 4(a) plots the Bode diagrams of the fitted 4th-, 6th-, and 10th-order rational function approximations (i.e., $Y^{low\_freq}_{vsc\_4th}$, $Y^{low\_freq}_{vsc\_6th}$, and $Y^{low\_freq}_{vsc\_10th}$) for the *dq*-domain AFRs of the VSC (i.e., Y_{vsc}) within low-frequency range [1, 100] Hz. It can be seen that $Y^{low\_freq}_{vsc\_4th}$ poorly captures the *qq*-axis AFRs close to 1 Hz, which can instead be accurately reproduced by $Y^{low\_freq}_{vsc\_6th}$ and $Y^{low\_freq}_{vsc\_10th}$. Figs. 4(b) and 4(c) plot the poles distribution and *qq*-axis residues distribution, respectively, of the VSC AFRs and the three rational function approximations. It can be seen that all the three rational function approximations can reproduce the in-band eigenvalue pairs $P(A_{1,2})$ and $P(B_{1,2})$. However, $Y^{low\_freq}_{vsc\_4th}$ cannot capture the in-band eigenvalue pair $P(C_{1,2})$, which can instead be accurately reproduced by $Y^{low\_freq}_{vsc\_6th}$ and $Y^{low\_freq}_{vsc\_10th}$.

In order to observe the over-fitting behavior of the MF, Fig. 5(a) plots the Bode diagrams of the fitted 6th-, 10th-, and 16th-order rational function approximations (i.e., $Y^{high\_freq}_{vsc\_6th}$, $Y^{high\_freq}_{vsc\_10th}$, and $Y^{high\_freq}_{vsc\_16th}$) for the *dq*-domain AFRs of the VSC (i.e., Y_{vsc}) within high-frequency range [101, 2500] Hz. It can be seen that the three rational function approximations can achieve almost the same in-band fitting capability. Figs. 5(b) and 5(c) plot the poles distribution and *qq*-axis residues distribution, respectively, of the VSC AFRs and the three rational function approximations. It can be seen that all the three rational function approximations can reproduce the in-band eigenvalue pairs (i.e., $P(D_{1,2})$ and $P(E_{1,2})$) and the out-of-band eigenvalue pair $P(A_{1,2})$. However, $Y^{high\_freq}_{vsc\_6th}$ cannot

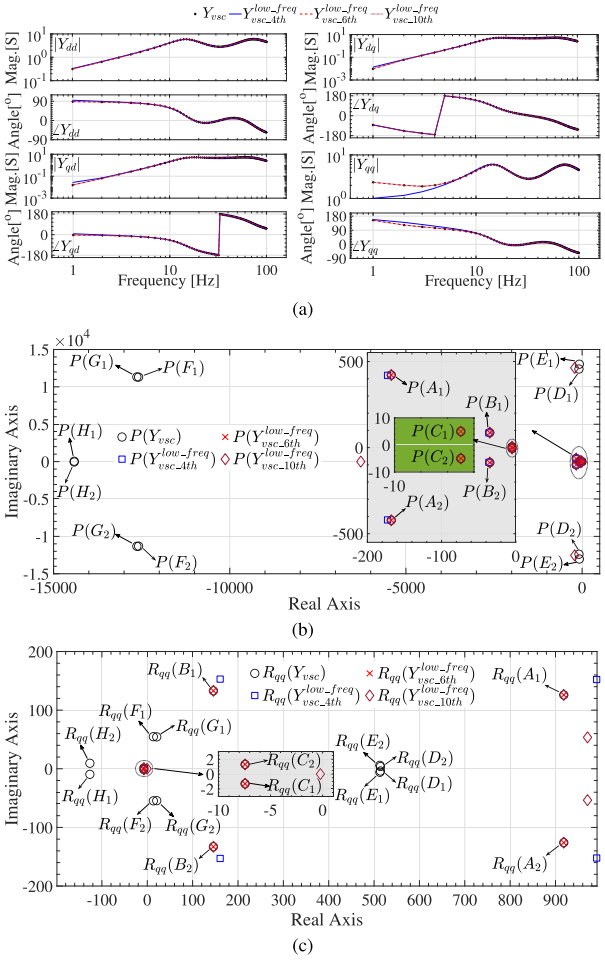

FIGURE 4. **(a) Bode plots, (b) poles distribution, and (c) *qq*-axis residues distribution of the fitted 4th-, 6th-, and 10th-order rational function approximations for the *dq*-domain AFRs of the VSC within [1, 100] Hz.**

capture the out-of-band eigenvalue pair $P(B_{1,2})$, which can instead be accurately reproduced by $Y^{high\_freq}_{vsc\_10th}$ and $Y^{high\_freq}_{vsc\_16th}$. As the best fitting scenario, $Y^{high\_freq}_{vsc\_16th}$ can capture all the in-band eigenvalue pairs (i.e., $P(D_{1,2})$, $P(E_{1,2})$, $P(F_{1,2})$, and $P(G_{1,2})$) and the out-of-band eigenvalue pairs (i.e., $P(A_{1,2})$, $P(B_{1,2})$, $P(C_{1,2})$, and $P(H_{1,2})$).

Compared to the extrapolation behavior of the VF on the artificially created rational function $H(s)$ in Fig. 2, it can be seen that the extrapolation behavior of the MF on the *dq*-domain AFRs of the VSC (i.e., Y_{vsc}) in Figs. 4 and 5 presents more interesting features. For example, as for the low-frequency fitting results in Fig. 4, $Y^{low\_freq}_{vsc\_10th}$ can capture the out-of-band eigenvalue pair $P(D_{1,2})$ instead of the in-band eigenvalue pair $P(H_{1,2})$. As for the high-frequency fitting results in Fig. 5, $Y^{high\_freq}_{vsc\_6th}$ can capture the out-of-band eigenvalue pair $P(A_{1,2})$ instead of the in-band eigenvalue pairs $P(F_{1,2})$ and $P(G_{1,2})$, while $Y^{high\_freq}_{vsc\_10th}$ can capture the out-of-band eigenvalue pairs $P(A_{1,2})$ and $P(B_{1,2})$ instead of the

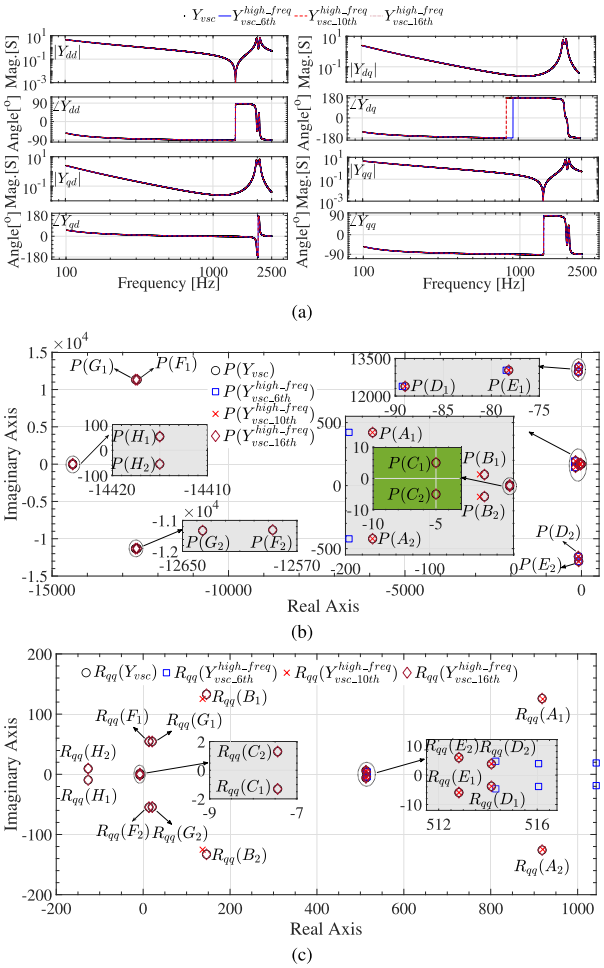

FIGURE 5. **(a) Bode plots, (b) poles distribution, and (c) *qq*-axis residues distribution of the fitted 6th-, 10th-, and 16th-order rational function approximations for the *dq*-domain AFRs of the VSC within [101, 2500] Hz.**

in-band eigenvalue pairs $P(F_{1,2})$ and $P(G_{1,2})$. These selective identification of the out-of-band eigenvalue pairs instead of the in-band eigenvalue pairs will further be investigated.

C. CLOSE LOOK AT THE EXTRAPOLATION BEHAVIOR FOR THE BLFRs

1) EXTRAPOLATION FOR THE ARTIFICIALLY CREATED FREQUENCY RESPONSE

If the fitting frequency interval is [2001, 8000] Hz, the artificially created rational function $H(s)$ in the form of (1) can be regarded as the summation of an in-band rational function $H_a(s)$ and an out-of-band rational function $H_b(s)$, i.e.,

$$H(s) = H_a(s) + H_b(s), \tag{8}$$

where

$$H_a(s) = \sum_{i=9}^{34} \frac{r_i}{s - p_i} + d,$$
$$H_b(s) = \sum_{i=1}^{8} \frac{r_i}{s - p_i} + \sum_{i=35}^{44} \frac{r_i}{s - p_i}, \tag{9}$$

where the pole and residue pair (p_i, r_i) are listed in Table 1. Fig. 6(a) plots the Bode diagrams of $H(s)$ in (1), $H_a(s)$ in (9), and $H_b(s)$ in (9). It can be seen that $H_a(s)$ can capture all the 13 (i.e., #5-#17) in-band amplitude peaks, while its out-of-band frequency response is smooth. On the contrary, $H_b(s)$ can capture all the 9 (i.e., #1-#4 and #18-#22) out-of-band amplitude peaks, while its in-band frequency response is smooth.

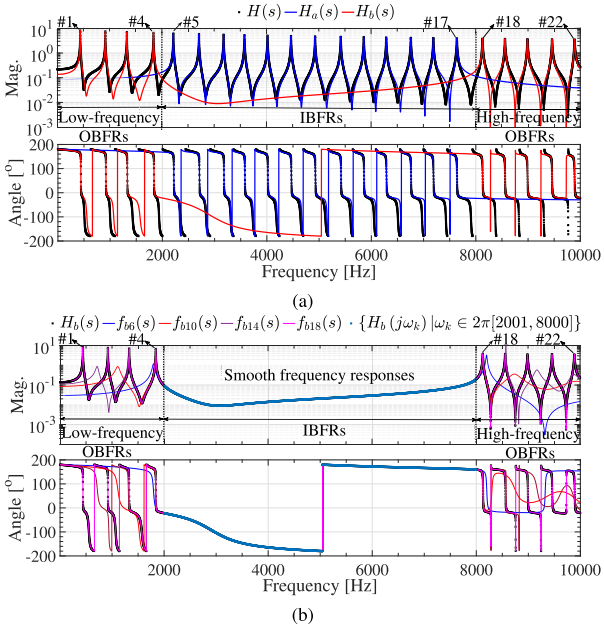

FIGURE 6. **Close look at the extrapolation behavior for the BLFRs of *H*(*s*) within [2001, 8000] Hz. (a) Bode plots of *H*(*s*), $H_a(s)$, and $H_b(s)$. (b) Bode plots of the fitted 6th-, 10th-, 14th-, and 18th-order rational function approximations (i.e., $f_{b6}(s)$, $f_{b10}(s)$, $f_{b14}(s)$, and $f_{b18}(s)$) for $\{H_b(j\omega_k)\,|\omega_k \in 2\pi[2001, 8000]\}$.**

When the frequency response $\{H(j\omega_k)|\omega_k \in 2\pi[2001, 8000]\}$ is fitted by the VF, the 26 partial fraction terms of $H_a(s)$ are preferentially identified, as shown in Fig. 2. If a high enough fitting order (e.g., 32th, 38th, and 44th in Fig. 2) is used, all the 26 partial fraction terms of $H_a(s)$ are captured and a few out-of-band partial fraction terms will be "guessed" to approximate the smoothed in-band fitting error $\{H_b(j\omega_k)\,|\omega_k \in 2\pi[2001, 8000]\}$. Assume that $\{H_b(j\omega_k)\,|\omega_k \in 2\pi[2001, 8000]\}$ is fitted by a N_1th-order rational function approximation $f_b(s)$, i.e.,

$$f_b(s)|_{s=j\omega_k} = \sum_{i=1}^{N_1} \frac{r_i'}{s - p_i'} \approx H_b(j\omega_k), \tag{10}$$

where p_i' and r_i' are the ith pole and residue pair of $f_b(s)$. Fig. 6(b) plots the Bode diagrams of the fitted 6th-, 10th-, 14th-, and 18th-order rational function approximations (i.e., $f_{b6}(s)$, $f_{b10}(s)$, $f_{b14}(s)$, and $f_{b18}(s)$) for $\{H_b(j\omega_k)\,|\omega_k \in 2\pi[2001, 8000]\}$, which indicates that both the low-frequency and high-frequency extrapolation performances improve if the fitting order N_1 is increased from 6th to 18th. Specifically, $f_{b18}(s)$ successfully identifies the nine

out-of-band partial fraction terms from the smoothed IBFRs of $\{H_b(j\omega_k)\,|\omega_k \in 2\pi[2001, 8000]\}$, which explains why the 44th-order ($44 = 26 + 18$) rational function approximation in Fig. 2 can reproduce the nine out-of-band partial fraction terms.

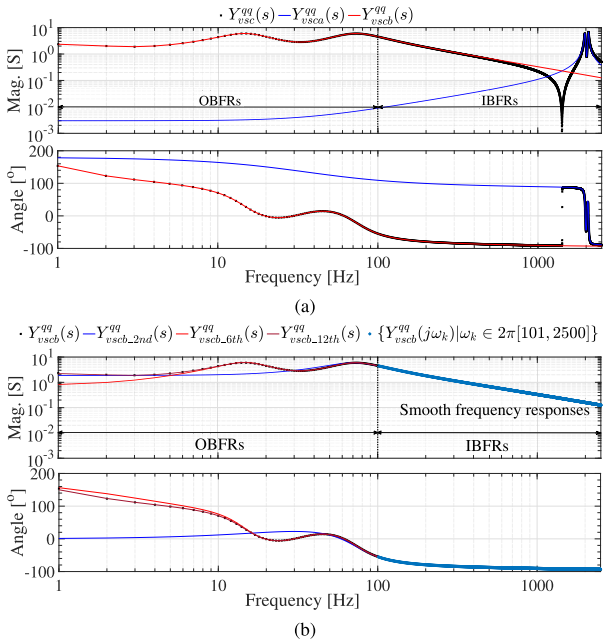

FIGURE 7. Close look at the extrapolation behavior for the BLFRs of $Y^{qq}_{vsc}(s)$ within [101, 2500] Hz. (a) Bode plots of $Y^{qq}_{vsc}(s)$, $Y^{qq}_{vsca}(s)$, and $Y^{qq}_{vscb}(s)$. (b) Bode plots of the fitted 2th-, 6th-, and 12th-order rational function approximations (i.e., $Y^{qq}_{vscb\_2nd}(s)$, $Y^{qq}_{vscb\_6th}(s)$, and $Y^{qq}_{vscb\_12th}(s)$) for $\{Y^{qq}_{vscb}(j\omega_k)\,|\omega_k \in 2\pi[101, 2500]\}$.

2) EXTRAPOLATION FOR THE GRID-CONNECTED VSC SYSTEM

Based on the poles and residues of the dq-domain admittance model Y_{vsc} in Table 2, if the fitting frequency interval is [101, 2500] Hz, the qq-axis admittance model of the VSC can be regarded as the summation of an in-band rational function $Y^{qq}_{vsca}(s)$ and an out-of-band rational function $Y^{qq}_{vscb}(s)$, i.e.,

$$Y^{qq}_{vsc}(s) = Y^{qq}_{vsca}(s) + Y^{qq}_{vscb}(s), \tag{11}$$

where

$$\begin{aligned} Y^{qq}_{vsca}(s) &= \frac{R_{qq}(D_{1,2})}{s - P(D_{1,2})} + \frac{R_{qq}(E_{1,2})}{s - P(E_{1,2})} \\ &\quad + \frac{R_{qq}(F_{1,2})}{s - P(F_{1,2})} + \frac{R_{qq}(G_{1,2})}{s - P(G_{1,2})}, \\ Y^{qq}_{vscb}(s) &= \frac{R_{qq}(A_{1,2})}{s - P(A_{1,2})} + \frac{R_{qq}(B_{1,2})}{s - P(B_{1,2})} \\ &\quad + \frac{R_{qq}(C_{1,2})}{s - P(C_{1,2})} + \frac{R_{qq}(H_{1,2})}{s - P(H_{1,2})}, \end{aligned} \tag{12}$$

where $P(\cdot)$ denotes the poles operator and $R_{qq}(\cdot)$ denotes the qq-axis residues operator. Fig. 7(a) plots the Bode diagrams of $Y^{qq}_{vsc}(s)$, $Y^{qq}_{vsca}(s)$ in (12), and $Y^{qq}_{vscb}(s)$ in (12). It can be seen that $Y^{qq}_{vsca}(s)$ can capture the magnitude peaks above 101 Hz, while its low-frequency spectrum below 101 Hz is smooth. On the contrary, $Y^{qq}_{vscb}(s)$ can capture the magnitude peaks below 101 Hz, while its high-frequency spectrum above 101 Hz is smooth.

Fig. 7(b) plots the Bode diagrams of the fitted 2nd-, 6th-, and 12th-order rational function approximations (i.e., $Y^{qq}_{vscb\_2nd}(s)$, $Y^{qq}_{vscb\_6th}(s)$, and $Y^{qq}_{vscb\_12th}(s)$) for $\left\{Y^{qq}_{vscb}(j\omega_k)\,|\omega_k \in 2\pi[101, 2500]\right\}$, which indicates that the low-frequency extrapolation performance improves if the fitting order is increased from 2nd to 12th. Specifically, $Y^{qq}_{vscb\_12th}(s)$ successfully reproduces the low-frequency AFRs from the smoothed IBFRs above 101 Hz, which explains why the 16th-order rational function approximation $Y^{high\_freq}_{vsc\_16th}$ in Fig. 5 can reproduce the out-of-band partial fraction terms (i.e., $A_{1,2}$, $B_{1,2}$, $C_{1,2}$, and $H_{1,2}$).

It can be seen that similar in-band fitting errors can be obtained by unions of different "guessed" out-of-band partial fraction terms, shown as $f_{b6}(s)$, $f_{b10}(s)$, $f_{b14}(s)$, and $f_{b18}(s)$ in Fig. 6 and $Y^{qq}_{vscb\_2nd}(s)$, $Y^{qq}_{vscb\_6th}(s)$, and $Y^{qq}_{vscb\_12th}(s)$ in Fig. 7. The internal mechanism of the selective and accurate out-of-band modal identification will be studied using the proposed sensitivity index.

III. PROPOSED SENSITIVITY INDEX OF THE PARTIAL FRACTION TERM

If a partial fraction term

$$G_0(s) = \frac{R_0}{s - P_0} = \frac{\alpha_0 + j\beta_0}{s - (\sigma_0 + j\omega_0)} \tag{13}$$

is identified as $G_{fit}(s) = R_{fit}/(s - P_{fit})$ by using the VF on K discrete frequency samples of $G_0(s)$ (i.e., $\{G_0(j\omega_k)\,|k = 1, 2, \ldots, K\}$), the in-band fitting error denoted as $\varepsilon(P_{fit}, R_{fit})$ can be calculated as

$$\varepsilon(P_{fit}, R_{fit}) = \sqrt{\left(\sum_{k=1}^{K}\left(G_{fit}(j\omega_k) - G_0(j\omega_k)\right)^2\right)/K}. \tag{14}$$

If the frequency samples number K is large enough, (14) can be reformulated as

$$\varepsilon^2(P_{fit}, R_{fit}) = \frac{1}{\omega_u - \omega_l}\int_{\omega_l}^{\omega_u}\left(G_{fit}(j\omega) - G_0(j\omega)\right)^2 d\omega, \tag{15}$$

which can be further reformulated as

$$\begin{aligned} \varepsilon^2(P_{fit}, R_{fit}) = \frac{1}{\omega_u - \omega_l}\int_{\omega_l}^{\omega_u} & G^2_{fit}(j\omega) - G^2_0(j\omega)\ldots \\ & -2G_0(j\omega)\left(G_{fit}(j\omega) - G_0(j\omega)\right)d\omega, \end{aligned} \tag{16}$$

where ω_l and ω_u denote the low-frequency and high-frequency limits, respectively, of the fitting frequency interval.

Using the first-order Taylor series expansion of $G_{fit}(j\omega)$ at (P_0, R_0) leads to

$$G_{fit}(j\omega) = G_0(j\omega) + \frac{R_{fit} - R_0}{j\omega - P_0} + \frac{R_0\left(P_{fit} - P_0\right)}{(j\omega - P_0)^2} + o^n, \tag{17}$$

where o^n is the higher-order infinitesimal. Since $P_{fit} \approx P_0$ and $R_{fit} \approx R_0$, one can have that

$$\begin{aligned}\frac{R_{fit} - R_0}{j\omega - P_0} &= \frac{R_{fit}}{R_0}G_0(j\omega) - G_0(j\omega)\\ &\approx \frac{R_{fit}}{R_{fit}}G_{fit}(j\omega) - G_0(j\omega),\\ \frac{R_0\left(P_{fit} - P_0\right)}{(j\omega - P_0)^2} &= \frac{P_{fit}}{R_0}G_0^2(j\omega) - \frac{P_0}{R_0}G_0^2(j\omega)\\ &\approx \frac{P_{fit}}{R_{fit}}G_{fit}^2(j\omega) - \frac{P_0}{R_0}G_0^2(j\omega).\end{aligned} \tag{18}$$

By substituting (18) into (17), one can have that

$$\begin{aligned}G_{fit}(j\omega) - G_0(j\omega) \approx \frac{R_{fit}G_{fit}(j\omega) + P_{fit}G_{fit}^2(j\omega)}{R_{fit}}\\ - \frac{R_0G_0(j\omega) + P_0G_0^2(j\omega)}{R_0}.\end{aligned} \tag{19}$$

Substituting (19) as a whole into (16) leads to

$$\varepsilon^2\left(P_{fit}, R_{fit}\right) \approx \zeta\left(P_{fit}, R_{fit}\right) - \zeta(P_0, R_0), \tag{20}$$

where

$$\begin{aligned}\zeta\left(P_{fit}, R_{fit}\right) = \frac{1}{\omega_u - \omega_l}\int_{\omega_l}^{\omega_u} G_{fit}^2(j\omega) - 2G_0(j\omega)\ldots\\ \left(G_{fit}(j\omega) + \frac{P_{fit}}{R_{fit}}G_{fit}^2(j\omega)\right)d\omega\end{aligned} \tag{21}$$

and

$$\begin{aligned}\zeta(P_0, R_0) = \frac{1}{\omega_u - \omega_l}\int_{\omega_l}^{\omega_u} G_0^2(j\omega) - 2G_0(j\omega)\ldots\\ \left(G_0(j\omega) + \frac{P_0}{R_0}G_0^2(j\omega)\right)d\omega.\end{aligned} \tag{22}$$

Since $G_0(j\omega) \approx G_{fit}(j\omega)$, substituting $G_{fit}(j\omega) = R_{fit}/(j\omega - P_{fit})$ into (21) leads to

$$\zeta\left(P_{fit}, R_{fit}\right) = -\frac{R_{fit}^2}{\omega_u - \omega_l}\int_{\omega_l}^{\omega_u}\frac{j\omega + P_{fit}}{\left(j\omega - P_{fit}\right)^3}d\omega. \tag{23}$$

In addition, substituting $G_0(j\omega) = R_0/(j\omega - P_0)$ into (22) leads to

$$\zeta(P_0, R_0) = -\frac{R_0^2}{\omega_u - \omega_l}\int_{\omega_l}^{\omega_u}\frac{j\omega + P_0}{(j\omega - P_0)^3}d\omega. \tag{24}$$

Using the first-order Taylor series expansion of $\zeta\left(P_{fit}, R_{fit}\right)$ at (P_0, R_0) can reformulate (20) as

$$\begin{aligned}\varepsilon^2\left(P_{fit}, R_{fit}\right) \approx \left(P_{fit} - P_0\right)\zeta_P'(P_0, R_0)\\ + \left(R_{fit} - R_0\right)\zeta_R'(P_0, R_0),\end{aligned} \tag{25}$$

where

$$\zeta_P'(P_0, R_0) = \frac{2R_0^2}{\omega_u - \omega_l}\left(\frac{\omega_u}{(j\omega_u - P_0)^3} - \frac{\omega_l}{(j\omega_l - P_0)^3}\right) \tag{26}$$

and

$$\zeta_R'(P_0, R_0) = \frac{2R_0}{\omega_u - \omega_l}\left(\frac{\omega_u}{(j\omega_u - P_0)^2} - \frac{\omega_l}{(j\omega_l - P_0)^2}\right), \tag{27}$$

indicate how sensitive the in-band fitting error $\varepsilon\left(P_{fit}, R_{fit}\right)$ is to the identified pole P_{fit} and the identified residue R_{fit}, respectively. In other words, the two sensitivity indexes are able to quantify the in-band fitting inaccuracy induced by specific reproduction inaccuracy of P_0 and R_0.

As a supplementary tool for the conventional fitting order selection method based on gradually increasing the fitting order until the root-mean-square fitting error defined in (14) is small enough, the proposed sensitivity index concept may help confirm the fitting order by checking if the sensitivity index of the last identified partial fraction term is obviously smaller than the sensitivity indexes of the already identified partial fraction terms.

Fig. 8 demonstrates the effects of P_0 and R_0 on $\left|\zeta_P'(P_0, R_0)\right|$ shown in (26). Specifically, Fig. 8(a) plots $\left|\zeta_P'(P_0, R_0)\right|$ variation as $\omega_u = 2\pi 8000$ rad/s, $\omega_l = 2\pi 2001$ rad/s, $\sigma_0 = -500$, $\alpha_0 = -10$, ω_0 is increased from 0 to $2\pi 10000$ rad/s, and β_0 is increased from 0 to 1000. Clearly, $\left|\zeta_P'(P_0, R_0)\right|$ is quickly increased if ω_0 goes close to ω_u or ω_l. Furthermore, $\left|\zeta_P'(P_0, R_0)\right|$ is increased if β_0 goes far from 0. A local minimal appears at about $2\pi 4500$ rad/s, indicating that if a mode with 4500-Hz amplitude peak is mixed with other in-band modes, this 4500-Hz mode may be not likely to be reproduced from the IBFRs within [2001, 8000] Hz, since the overall in-band fitting inaccuracy is not sensitive to the reproduction precision of this 4500-Hz mode. Furthermore, Fig. 8(b) plots $\left|\zeta_P'(P_0, R_0)\right|$ variation as $\omega_0 = 2\pi 8050$ rad/s, $\beta_0 = 1000$, σ_0 is increased from -1000 to 0, and α_0 is increased from -400 to 0. Clearly, $\left|\zeta_P'(P_0, R_0)\right|$ is increased as σ_0 approaches 0 and decreased as α_0 approaches 0.

IV. VERIFICATION OF SENSITIVITY INDEX ON THE ARTIFICIALLY CREATED RATIONAL FUNCTION

A. IN-BAND FITTING FOR THE ARTIFICIALLY CREATED RATIONAL FUNCTIONS

1) ARTIFICIALLY CREATED RATIONAL FUNCTIONS COMPOSED OF TWO PARTIAL FRACTION TERMS

Fig. 9(a) plots the Bode diagrams of the fitted five first-order approximations $h_m^{fit}(s)$ where m can be 5500, 6000, 6500, 7000, and 7500 for

$$h_m(s) = \frac{-10 + j1000}{s - (-500 + j2\pi 4500)} + \frac{-10 + j1000}{s - (-500 + j2\pi m)}, \tag{28}$$

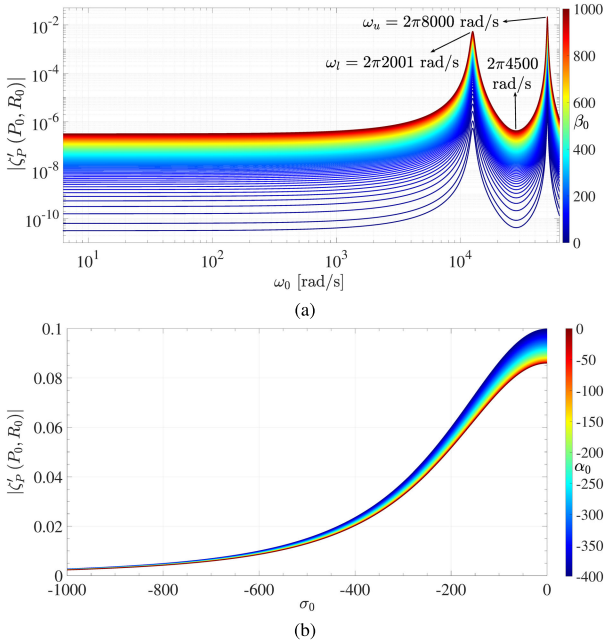

FIGURE 8. Variation of the sensitivity index $\left|\zeta'_P(P_0, R_0)\right|$ as (a) ω_0 and β_0, and (b) σ_0 and α_0 change.

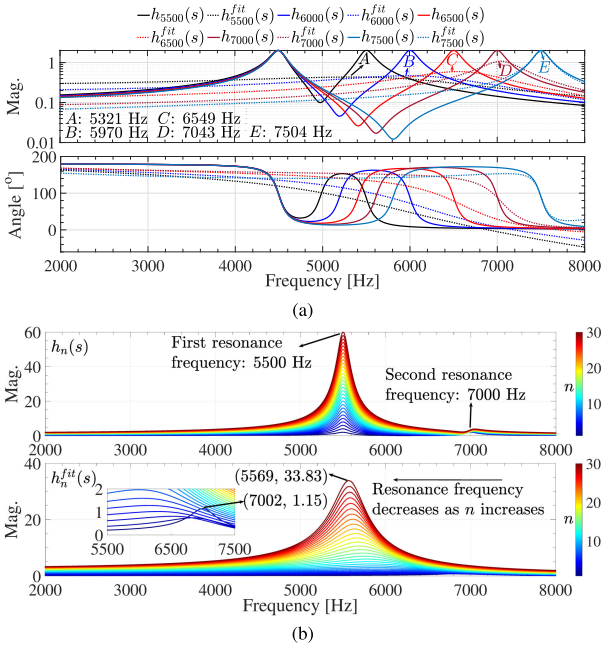

FIGURE 9. The fitted first-order approximation (a) $h_m^{fit}(s)$ for $h_m(s)$ and (b) $h_n^{fit}(s)$ for $h_n(s)$ based on the frequency responses between 2001 and 8000 Hz.

based on the frequency responses between 2001 and 8000 Hz. It can be seen that the amplitude peaks of the fitted five first-order rational functions are situated at 5321, 5970, 6549, 7043, and 7504 Hz, respectively. Compared to the amplitude peak of the 4500-Hz mode in (28), the reproduced five amplitude peaks are clearly much closer to the five amplitude peaks of the m-Hz modes. Specifically, the fitted $h_{7500}^{fit}(s)$ nearly completely captures the 7500-Hz amplitude peak of $h_{7500}(s)$, which is due to that $\left|\zeta'_P(P_0, R_0)\right|$ sharply increases when ω_0 varies from $2\pi 4500$ rad/s to $2\pi 7500$ rad/s, as shown in Fig. 8(a). Therefore, the feasibility of the derived sensitivity index $\left|\zeta'_P(P_0, R_0)\right|$ in (26) is verified.

Furthermore, Fig. 9(b) plots the magnitude diagrams of the fitted first-order approximation $h_n^{fit}(s)$ where n is increased from 1 to 30 with step size 1 for

$$h_n(s) = \frac{n(-10 + j1000)}{s - (-500 + j2\pi 5500)} + \frac{-10 + j1000}{s - (-500 + j2\pi 7000)}, \tag{29}$$

based on the frequency responses between 2001 and 8000 Hz. Clearly, the amplitude peak of the fitted first-order rational function $h_n^{fit}(s)$ moves leftward if n is increased. Specifically, the identified amplitude peak is located at 7002 Hz when $n = 1$ and at 5569 Hz when $n = 30$, which results from that the sensitivity index of the 5500-Hz mode is increased if n is increased, i.e., $\left|\zeta'_P(P_0, R_0)\right|$ is increased as $|R_0|$ increases as shown in Fig. 8. Therefore, the feasibility of the derived sensitivity index $\left|\zeta'_P(P_0, R_0)\right|$ in (26) is verified.

2) ARTIFICIALLY CREATED RATIONAL FUNCTION COMPOSED OF MULTIPLE PARTIAL FRACTION TERMS

When the fitting frequency interval is [3001, 7000] Hz, the sensitivity indexes of the 22 pairs of modes of $H(s)$ shown in Table 1 can be calculated by (26), as listed in the second and third columns in Table 3. It can be observed that the distribution of these sensitivity indexes agrees with that shown in Fig. 8(a). Specifically, the #16 and #7 magnitude peaks have the largest and the second largest sensitivity index, respectively, which indicates that the #16 and #7 magnitude peaks are the most and the second most likely to be identified from the BLFRs within [3001, 7000] Hz. The sensitivity index-based fitting behavior prediction agrees with the practical fitting results shown in Fig. 1. Therefore, the feasibility of the derived sensitivity index is validated.

B. EXTRAPOLATION FOR THE ARTIFICIALLY CREATED RATIONAL FUNCTIONS

1) ARTIFICIALLY CREATED RATIONAL FUNCTION COMPOSED OF TWO PARTIAL FRACTION TERMS

Assume that the first-order approximation

$$h_t^{fit}(s) = \frac{R_t^{fit}}{s - P_t^{fit}} = \frac{\alpha_t^{fit} + j\beta_t^{fit}}{s - \left(\sigma_t^{fit} + j\omega_t^{fit}\right)} \tag{30}$$

fits the summation of the IBFRs of

$$h_{t1}(s) = \frac{R_{t1}}{s - P_{t1}} = \frac{\alpha_{t1} + j\beta_{t1}}{s - (\sigma_{t1} + j\omega_{t1})} \tag{31}$$

TABLE 3. Sensitivity Indexes of the Partial Fraction Terms of $H(s)$ Shown in Table 1.

Term $\#i$	$\omega_l = 2\pi 3001$ rad/s, $\omega_u = 2\pi 7000$ rad/s $\lvert\zeta'_P(P_i,R_i)\rvert$	$\lvert\zeta'_R(P_i,R_i)\rvert$	$\omega_l = 2\pi 2001$ rad/s, $\omega_u = 2\pi 8000$ rad/s $\lvert\zeta'_P(P_i,R_i)\rvert$	$\lvert\zeta'_R(P_i,R_i)\rvert$
#1	2.1111×10^{-9}	3.0820×10^{-7}	4.6448×10^{-9}	4.7475×10^{-7}
#2	4.2657×10^{-9}	5.3420×10^{-7}	1.4727×10^{-8}	1.0987×10^{-6}
#3	8.8008×10^{-9}	9.2253×10^{-7}	6.4149×10^{-8}	3.0649×10^{-6}
#4	2.7977×10^{-8}	2.1452×10^{-6}	4.8658×10^{-6}	5.6651×10^{-5}
#5	9.6267×10^{-8}	5.1168×10^{-6}	1.9265×10^{-6}	3.0301×10^{-5}
#6	1.9448×10^{-6}	3.9599×10^{-5}	5.9516×10^{-8}	2.7541×10^{-6}
#7	8.3693×10^{-6}	1.0479×10^{-4}	1.3979×10^{-8}	8.2840×10^{-7}
#8	2.6010×10^{-7}	9.5981×10^{-6}	6.6872×10^{-9}	3.0125×10^{-7}
#9	5.3142×10^{-8}	2.4506×10^{-6}	4.2349×10^{-9}	1.1728×10^{-8}
#10	2.4314×10^{-8}	3.4952×10^{-7}	3.7041×10^{-9}	2.4832×10^{-7}
#11	2.1887×10^{-8}	9.9520×10^{-7}	4.3055×10^{-9}	4.9331×10^{-7}
#12	3.7005×10^{-8}	2.7904×10^{-6}	6.4064×10^{-9}	8.3676×10^{-7}
#13	9.2814×10^{-8}	6.1924×10^{-6}	1.0851×10^{-8}	1.3263×10^{-6}
#14	3.8554×10^{-7}	1.7008×10^{-5}	2.1268×10^{-8}	2.1890×10^{-6}
#15	1.0196×10^{-5}	1.5355×10^{-4}	5.6588×10^{-8}	4.3167×10^{-6}
#16	2.1071×10^{-5}	2.4831×10^{-4}	2.0754×10^{-7}	1.0359×10^{-5}
#17	5.6514×10^{-7}	2.2010×10^{-5}	2.4219×10^{-6}	5.3376×10^{-5}
#18	1.0491×10^{-7}	7.0581×10^{-6}	5.2653×10^{-5}	4.1445×10^{-4}
#19	4.0673×10^{-8}	3.6999×10^{-6}	6.7615×10^{-7}	2.2597×10^{-5}
#20	1.9953×10^{-8}	2.2694×10^{-6}	1.2535×10^{-7}	7.2964×10^{-6}
#21	1.0734×10^{-8}	1.4798×10^{-6}	3.9995×10^{-8}	3.3803×10^{-6}
#22	6.7261×10^{-9}	1.0698×10^{-6}	1.8855×10^{-8}	2.0317×10^{-6}

and

$$h_{t2}(s) = \frac{R_{t2}}{s - P_{t2}} = \frac{\alpha_{t2} + j\beta_{t2}}{s - (\sigma_{t2} + j\omega_{t2})} \tag{32}$$

in the frequency interval $[0, \omega_u]$. According to (25), the in-band fitting inaccuracy $\varepsilon^2\left(P_t^{fit}, R_t^{fit}\right)$ induced by the inaccurate reproduction of ω_{t1} in (31) and ω_{t2} in (32) can be calculated as

$$\varepsilon^2\left(P_t^{fit}, R_t^{fit}\right) = \left(\omega_t^{fit} - \omega_{t1}\right)\zeta'_P(P_{t1}, R_{t1}) + \left(\omega_t^{fit} - \omega_{t2}\right)\zeta'_P(P_{t2}, R_{t2}). \tag{33}$$

Solving $\varepsilon^2\left(P_t^{fit}, R_t^{fit}\right) = 0$ leads to

$$\omega_t^{fit} = \frac{\omega_{t1}\zeta'_P(P_{t1}, R_{t1}) + \omega_{t2}\zeta'_P(P_{t2}, R_{t2})}{\zeta'_P(P_{t1}, R_{t1}) + \zeta'_P(P_{t2}, R_{t2})} \in (\omega_{t1}, \omega_{t2}), \tag{34}$$

where three cases can be summarized in Table 4. By substituting (26) into (34), it can be derived that if

$$\frac{\alpha_{t1}^2 + \beta_{t1}^2}{\alpha_{t2}^2 + \beta_{t2}^2} = \left(\frac{\sigma_{t1}^2 + (\omega_{t1} - \omega_u)^2}{\sigma_{t2}^2 + (\omega_{t2} - \omega_u)^2}\right)^{\frac{3}{2}}, \tag{35}$$

case 2 in Table 4 holds, and the captured amplitude peak ω_t^{fit} is situated at the midpoint of $(\omega_{t1}, \omega_{t2})$. Specifically, if $R_{t2} = \gamma_t R_{t1}$, γ_t should be

$$\gamma_t = \left(\frac{\sigma_{t2}^2 + (\omega_{t2} - \omega_u)^2}{\sigma_{t1}^2 + (\omega_{t1} - \omega_u)^2}\right)^{\frac{3}{4}}, \tag{36}$$

such that case 2 is satisfied.

Consider a case where $P_{t1} = -40 + j2\pi 1200$, $R_{t1} = 20 + j1600$, $P_{t2} = -40 + j2\pi 1300$, $R_{t2} = \gamma_t R_{t1}$, and $\omega_u = 2\pi 1000$ rad/s. Fig. 10(a) plots the Bode diagram of the fitted rational function $h_t^{fit}(s)$ as γ_t is increased from 1.0 to 3.0 with step size 0.1. The captured amplitude peak ω_t^{fit} clearly moves toward to $2\pi 1300$ Hz when γ_t is increased. Specifically, the captured amplitude peak ω_t^{fit} is situated at 1250 Hz if γ_t is nearly 2.0. Since γ_t calculated by (36) is 1.8, the discrepancy between the γ_t obtained by the VF and (36) is small, which verifies the feasibility of the derived sensitivity index.

TABLE 4. Location of the Identified Magnitude Peak of $h_t^{fit}(s)$.

	$\zeta'_P(P_{t1}, R_{t1})$? $\zeta'_P(P_{t2}, R_{t2})$	ω_t^{fit}
Case 1	$>$	$(\omega_{t1}, \frac{\omega_{t1}+\omega_{t2}}{2})$
Case 2	$=$	$\frac{\omega_{t1}+\omega_{t2}}{2}$
Case 3	$<$	$(\frac{\omega_{t1}+\omega_{t2}}{2}, \omega_{t2})$

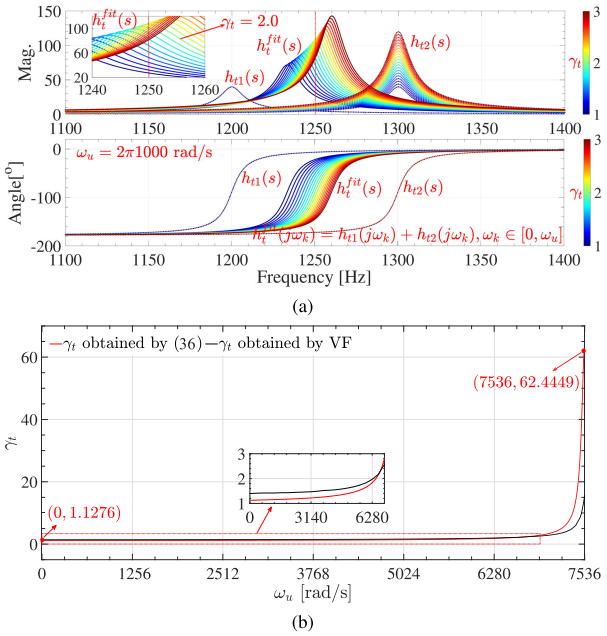

FIGURE 10. (a) Variation of the captured amplitude peak of $h_t^{fit}(s)$ when ω_u is $2\pi 1000$ rad/s and γ_t is increased from 1.0 to 3.0 with step size 0.1. (b) Variation of γ_t as ω_u is increased from 0 to $2\pi 1200$ rad/s.

Furthermore, Fig. 10(b) plots γ_t variation calculated by (36) as ω_u increases from 0 to $2\pi 1200$ rad/s. It can be seen that γ_t slowly decreases and quickly increases to 1.1276 and 62.4449 if ω_u approaches 0 and $2\pi 1200$ rad/s, respectively, which indicates that the out-of-band magnitude peak located at the edge of the fitting frequency interval is most likely to be identified among all the out-of-band magnitude peaks. The discrepancies between the γ_t obtained by (36) and the VF code below 1100 Hz are small and acceptable, which verifies the feasibility of the derived sensitivity index.

2) ARTIFICIALLY CREATED RATIONAL FUNCTION COMPOSED OF MULTIPLE PARTIAL FRACTION TERMS

When the fitting frequency interval is [2001, 8000] Hz, the sensitivity indexes of the 22 pairs of partial fraction terms of $H(s)$ shown in Table 1 can be calculated by (26), as listed in the fourth and fifth columns in Table 3. It can be observed that the distribution of theses sensitivity indexes agree with that shown in Fig. 8(a). Specifically, the #18 and #4 magnitude

peaks have the largest and the second largest sensitivity index, respectively. It indicates that, in the left-side out-of-band frequency interval, the reproduction priority is #4, #3, #2, and #1. In addition, in the right-side out-of-band frequency interval, the reproduction priority is #18, #19, #20, #21, and #22. The sensitivity index-based fitting behavior prediction agrees with the practical fitting results shown in Fig. 2. Therefore, the feasibility of the derived sensitivity index is validated.

V. VERIFICATION OF SENSITIVITY INDEX ON THE VSCs

A. THE CURRENT-CONTROLLED VSC

1) LOW-FREQUENCY FITTING FOR THE CURRENT-CONTROLLED VSC WITHIN [1, 100] Hz

The sensitivity indexes of the 8 pairs of partial fraction terms when the fitting frequency interval is [1, 100] Hz are listed in the second and third columns in Table 5. It can be observed that $A_{1,2}$, $B_{1,2}$, $C_{1,2}$, and $D_{1,2}$ have the largest, second largest, third largest, and fourth largest sensitivity indexes, respectively, which indicates that they are the most, second most, third most, and fourth most likely to be identified from the BLFRs within [1, 100] Hz. The sensitivity index-based fitting behavior prediction agrees with the practical fitting results shown in Fig. 4. In addition, it can be seen that although $H_{1,2}$ are located within the fitting frequency interval, its sensitivity index is smaller than that of $D_{1,2}$. This explains why $D_{1,2}$ instead of $H_{1,2}$ are identified by $Y_{vsc\_10th}^{low\_freq}$ in Fig. 4. The effectiveness of the proposed sensitivity index is thus verified.

TABLE 5. Sensitivity Indexes of the Partial Fraction Terms of $Y_{vsc}^{qq}(s)$ When the Low- and High-Frequency Responses are Fitted.

Term i	$\omega_l = 2\pi 1$ rad/s, $\omega_u = 2\pi 100$ rad/s		$\omega_l = 2\pi 101$ rad/s, $\omega_u = 2\pi 2500$ rad/s	
	$\lvert\zeta'_P(P(i),R_{qq}(i))\rvert$	$\lvert\zeta'_R(P(i),R_{qq}(i))\rvert$	$\lvert\zeta'_P(P(i),R_{qq}(i))\rvert$	$\lvert\zeta'_R(P(i),R_{qq}(i))\rvert$
$A_{1,2}$	5.7398×10^{1}	1.6466×10^{1}	3.6000×10^{-3}	1.1000×10^{-3}
$B_{1,2}$	3.0703×10^{-1}	8.4342×10^{-1}	1.9830×10^{-5}	5.3520×10^{-5}
$C_{1,2}$	2.9654×10^{-4}	2.4450×10^{-2}	1.9231×10^{-8}	1.5411×10^{-6}
$D_{1,2}$	2.0413×10^{-4}	4.6692×10^{-3}	1.5054×10^{-5}	9.6840×10^{-5}
$E_{1,2}$	1.7317×10^{-4}	4.1878×10^{-3}	2.8519×10^{-5}	1.4864×10^{-4}
$F_{1,2}$	8.8556×10^{-7}	2.5958×10^{-4}	2.8471×10^{-9}	6.6875×10^{-7}
$G_{1,2}$	9.4059×10^{-7}	2.6712×10^{-4}	3.0247×10^{-9}	6.8815×10^{-7}
$H_{1,2}$	6.7357×10^{-6}	7.6579×10^{-4}	3.8161×10^{-9}	5.8638×10^{-7}

Note: $P(\cdot)$ denotes the poles operator. $R_{qq}(\cdot)$ denote the qq-axis residues operator.

2) HIGH-FREQUENCY FITTING FOR THE CURRENT-CONTROLLED VSC WITHIN [101, 2500] Hz

The sensitivity indexes of the 8 pairs of partial fraction terms when the fitting frequency interval is [101, 2500] Hz are listed in the fourth and fifth columns in Table 5. It can be observed that $A_{1,2}$, $E_{1,2}$, $D_{1,2}$, and $B_{1,2}$ have the largest, second largest, third largest, and fourth largest sensitivity index, respectively, which indicates that they are the most, second most, third most, and fourth most likely to be identified from the BLFRs within [101, 2500] Hz. The sensitivity index-based fitting behavior prediction agrees with the practical fitting results shown in Fig. 5. In addition, it can be seen that although $F_{1,2}$ and $G_{1,2}$ are located within the fitting frequency interval, their sensitivity indexes are smaller than those of $A_{1,2}$ and $B_{1,2}$. This explains why $A_{1,2}$ and $B_{1,2}$ instead of $F_{1,2}$ and $G_{1,2}$ are identified by $Y_{vsc\_10th}^{high\_freq}$ in Fig. 5. The effectiveness of the derived sensitivity index is thus validated. Thanks to that the proposed sensitivity index can explain why the out-of-band modes can be preferentially captured before the desired in-band modes are captured, the adopted fitting order which already satisfies the fitting error requirement can be further increased to identify more in-band modes. Therefore, a fitting order which can simultaneously satisfy the fitting error requirement and identify enough in-band modes can be obtained.

3) MIDDLE-FREQUENCY FITTING FOR THE CURRENT-CONTROLLED VSC WITHIN DIFFERENT FREQUENCY RANGES

The sensitivity indexes of the 8 pairs of partial fraction terms when the fitting frequency interval is [401, 700], [401, 1200], [401, 1700], and [401, 2200] Hz are listed in Table 6. It can be observed that, $A_{1,2}$ have the largest sensitivity index, and are most likely to be identified from the BLFRs within [401, 700] Hz. In addition, $A_{1,2}$ and $D_{1,2}$ have the largest and second largest sensitivity indexes, and are most and second most likely to be identified from the BLFRs within [401, 1200] Hz. $D_{1,2}$ have the largest sensitivity index, and are most likely to be identified from the BLFRs within [401, 1700] Hz. $E_{1,2}$ and $D_{1,2}$ have the largest and second largest sensitivity indexes, and are most and second most likely to be identified from the BLFRs within [401, 2200] Hz.

TABLE 6. Sensitivity Indexes of the Partial Fraction Terms of $Y_{vsc}^{qq}(s)$ When the Middle-Frequency Responses are Fitted.

Term i	$\omega_l = 2\pi 401$ rad/s, $\omega_u = 2\pi 700$ rad/s		$\omega_l = 2\pi 401$ rad/s, $\omega_u = 2\pi 1200$ rad/s	
	$\lvert\zeta'_P(P(i),R_{qq}(i))\rvert$	$\lvert\zeta'_R(P(i),R_{qq}(i))\rvert$	$\lvert\zeta'_P(P(i),R_{qq}(i))\rvert$	$\lvert\zeta'_R(P(i),R_{qq}(i))\rvert$
$A_{1,2}$	1.8395×10^{-4}	2.8886×10^{-4}	8.5468×10^{-5}	1.5560×10^{-4}
$B_{1,2}$	4.9801×10^{-6}	3.9735×10^{-5}	2.4325×10^{-6}	2.2800×10^{-5}
$C_{1,2}$	6.4792×10^{-9}	1.3723×10^{-6}	3.2036×10^{-9}	7.9973×10^{-7}
$D_{1,2}$	1.6887×10^{-6}	2.3548×10^{-5}	6.6886×10^{-6}	6.0385×10^{-5}
$E_{1,2}$	1.3071×10^{-6}	1.9775×10^{-5}	4.5454×10^{-6}	4.6438×10^{-5}
$F_{1,2}$	2.8838×10^{-9}	6.6690×10^{-7}	3.7616×10^{-9}	7.9994×10^{-7}
$G_{1,2}$	3.0541×10^{-9}	6.8488×10^{-7}	3.9802×10^{-9}	8.2096×10^{-7}
$H_{1,2}$	1.0484×10^{-8}	1.1459×10^{-6}	9.1778×10^{-9}	1.0201×10^{-6}
Term i	$\omega_l = 2\pi 401$ rad/s, $\omega_u = 2\pi 1700$ rad/s		$\omega_l = 2\pi 401$ rad/s, $\omega_u = 2\pi 2200$ rad/s	
	$\lvert\zeta'_P(P(i),R_{qq}(i))\rvert$	$\lvert\zeta'_R(P(i),R_{qq}(i))\rvert$	$\lvert\zeta'_P(P(i),R_{qq}(i))\rvert$	$\lvert\zeta'_R(P(i),R_{qq}(i))\rvert$
$A_{1,2}$	5.4858×10^{-5}	1.0639×10^{-4}	4.0231×10^{-5}	8.0803×10^{-5}
$B_{1,2}$	1.5843×10^{-6}	1.5986×10^{-5}	1.1691×10^{-6}	1.2307×10^{-5}
$C_{1,2}$	2.0943×10^{-9}	5.6430×10^{-7}	1.5479×10^{-9}	4.3596×10^{-7}
$D_{1,2}$	1.3848×10^{-4}	4.5757×10^{-4}	2.1766×10^{-4}	6.0600×10^{-4}
$E_{1,2}$	5.2914×10^{-5}	2.4023×10^{-4}	1.3000×10^{-3}	2.0000×10^{-3}
$F_{1,2}$	4.2397×10^{-9}	8.7385×10^{-7}	3.9692×10^{-9}	8.4719×10^{-7}
$G_{1,2}$	4.4875×10^{-9}	8.9690×10^{-7}	4.2086×10^{-9}	8.7046×10^{-7}
$H_{1,2}$	7.4768×10^{-9}	8.6836×10^{-7}	5.8912×10^{-9}	7.2451×10^{-7}

Note: $P(\cdot)$ denotes the poles operator. $R_{qq}(\cdot)$ denote the qq-axis residues operator.

Figs. 11(a) and 11(b) plot the poles distribution and qq-axis residues distribution, respectively, of the dq-domain AFRs of the VSC (i.e., Y_{vsc}) and its fitted 4th-order rational function approximations using the AFRs within [401, 700], [401, 1200], [401, 1700], and [401, 2200] Hz (i.e., $Y_{vsc\_4th}^{[401,700]}$, $Y_{vsc\_4th}^{[401,1200]}$, $Y_{vsc\_4th}^{[401,1700]}$, and $Y_{vsc\_4th}^{[401,2200]}$). It can be seen from Fig. 11(a) that only $P(A_{1,2})$ can be captured by $Y_{vsc\_4th}^{[401,700]}$. In addition, both $P(A_{1,2})$ and $P(D_{1,2})$ can be captured by $Y_{vsc\_4th}^{[401,1200]}$. Only $P(D_{1,2})$ can be captured by $Y_{vsc\_4th}^{[401,1700]}$. Both

$P(D_{1,2})$ and $P(E_{1,2})$ can be captured by $Y_{vsc\_4th}^{[401,2200]}$. The practical fitting results shown in Fig. 11 agree with the sensitivity index-based fitting behavior prediction shown in Table 6, which verifies the effectiveness of the derived sensitivity index.

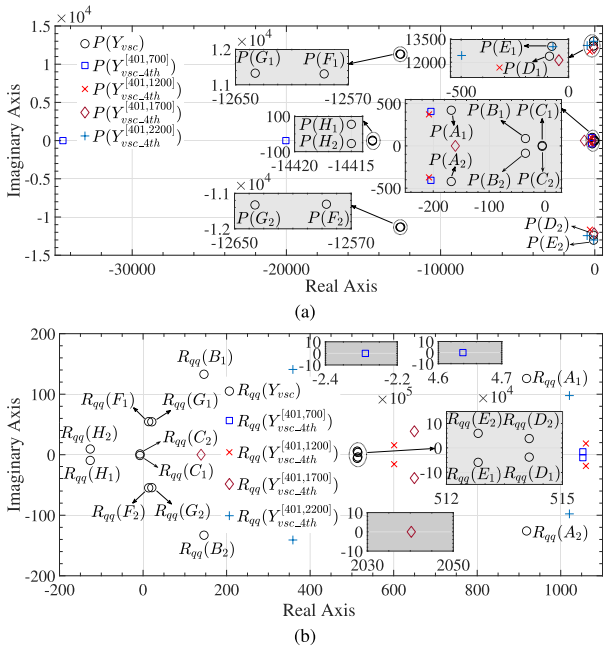

FIGURE 11. **(a) Poles distribution and (b) *qq*-axis residues distribution of the fitted 4th-order rational function approximations for the *dq*-domain AFRs of the VSC within [401, 700], [401, 1200], [401, 1700], and [401, 2200] Hz.**

B. THE VOLTAGE-CONTROLLED VSC

In order to verify the effectiveness of the proposed sensitivity index, the AFRs of the voltage-controlled VSC are further fitted by the MF. Fig. 12(a) shows the control diagram of the outer dc-link voltage control which is responsible for generating the d-axis current reference i_{2d}^{ref}, while Fig. 12(b) shows the control diagram of the outer PCC voltage control which is responsible for generating the q-axis current reference i_{2q}^{ref}. The voltage controller parameters are shown in Table 9 of Appendix.

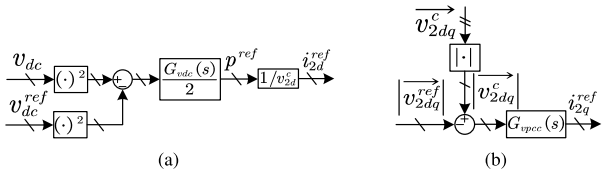

FIGURE 12. **Block diagrams of (a) dc-link voltage control and (b) PCC voltage control.**

Table 7 lists the poles and residues of the *dq*-domain AFRs of the voltage-controlled VSC (i.e., Y_{vc_vsc}). Compared to the poles and residues of the *dq*-domain AFRs of the current-controlled VSC (i.e., Y_{vsc}) in Table 2, it can be seen that Y_{vc_vsc} has additional partial fraction terms $I_{1,2}$ and J.

TABLE 7. **Poles and Residues of the *DQ*-Domain Admittance Transfer Function Matrix Y_{vc_vsc} of the Voltage-Controlled VSC.**

$P(Y_{vc\_vsc})$	$\begin{bmatrix} R_{dd}(Y_{vc\_vsc}) & R_{dq}(Y_{vc\_vsc}) \\ R_{qd}(Y_{vc\_vsc}) & R_{qq}(Y_{vc\_vsc}) \end{bmatrix}$
$P(A_{1,2})$: $(-95.179 \pm j208.49)$	$\begin{bmatrix} R_{dd}(A_{1,2}) & R_{dq}(A_{1,2}) \\ R_{qd}(A_{1,2}) & R_{qq}(A_{1,2}) \end{bmatrix}$: $\begin{bmatrix} -35.6224 \mp j455.9194 & -3033.4 \pm j1356.6 \\ -179.7672 \pm j110.3951 & 1194.3 \pm j960.8797 \end{bmatrix}$
$P(B_{1,2})$: $(-128.24 \pm j81.311)$	$\begin{bmatrix} R_{dd}(B_{1,2}) & R_{dq}(B_{1,2}) \\ R_{qd}(B_{1,2}) & R_{qq}(B_{1,2}) \end{bmatrix}$: $\begin{bmatrix} 416.5808 \mp j3.0388 & -137.6932 \mp j602.7674 \\ -20.7467 \pm j30.8026 & 51.2796 \pm j20.2121 \end{bmatrix}$
$P(C_{1,2})$: $(-4.3478 \pm j4.9573)$	$\begin{bmatrix} R_{dd}(C_{1,2}) & R_{dq}(C_{1,2}) \\ R_{qd}(C_{1,2}) & R_{qq}(C_{1,2}) \end{bmatrix}$: $\begin{bmatrix} 0 \pm 0 & -0.0669 \mp j0.1146 \\ 0 \pm 0 & -3.4518 \mp j0.6757 \end{bmatrix}$
$P(D_{1,2})$: $(-48.921 \pm j12436)$	$\begin{bmatrix} R_{dd}(D_{1,2}) & R_{dq}(D_{1,2}) \\ R_{qd}(D_{1,2}) & R_{qq}(D_{1,2}) \end{bmatrix}$: $\begin{bmatrix} 514.2014 \mp j94.7268 & 215.8204 \pm j677.2104 \\ 50.2183 \mp j372.6757 & 511.1803 \pm j3.8892 \end{bmatrix}$
$P(E_{1,2})$: $(-130.7557 \pm j13004)$	$\begin{bmatrix} R_{dd}(E_{1,2}) & R_{dq}(E_{1,2}) \\ R_{qd}(E_{1,2}) & R_{qq}(E_{1,2}) \end{bmatrix}$: $\begin{bmatrix} 602.9088 \pm j6.8841 & -211.2731 \mp j636.5213 \\ -137.5384 \pm j439.7659 & 512.3113 \mp j14.7475 \end{bmatrix}$
$P(F_{1,2})$: $(-12242 \pm j11706)$	$\begin{bmatrix} R_{dd}(F_{1,2}) & R_{dq}(F_{1,2}) \\ R_{qd}(F_{1,2}) & R_{qq}(F_{1,2}) \end{bmatrix}$: $\begin{bmatrix} 68.7024 \pm j87.7240 & -1.6641 \pm j66.6062 \\ 101.8630 \pm j136.1803 & -4.7928 \pm j101.5763 \end{bmatrix}$
$P(G_{1,2})$: $(-13150 \pm j10910)$	$\begin{bmatrix} R_{dd}(G_{1,2}) & R_{dq}(G_{1,2}) \\ R_{qd}(G_{1,2}) & R_{qq}(G_{1,2}) \end{bmatrix}$: $\begin{bmatrix} 476.3558 \pm j369.0923 & -14.5815 \pm j1.6281 \\ -606.9094 \mp j459.1695 & 18.3899 \mp j2.2679 \end{bmatrix}$
$P(H_{1,2})$: $-15512, -12897$	$\begin{bmatrix} R_{dd}(H_{1,2}) & R_{dq}(H_{1,2}) \\ R_{qd}(H_{1,2}) & R_{qq}(H_{1,2}) \end{bmatrix}$: $\begin{bmatrix} -223.1557, -1507.7 & -145.9618, -30.4402 \\ -344.6388, 1926.0 & -225.4216, 38.8862 \end{bmatrix}$
$P(I_{1,2})$: $(-8.5352 \pm j274.22)$	$\begin{bmatrix} R_{dd}(I_{1,2}) & R_{dq}(I_{1,2}) \\ R_{qd}(I_{1,2}) & R_{qq}(I_{1,2}) \end{bmatrix}$: $\begin{bmatrix} 827.6085 \pm j1185.3 & 3187.6 \pm j117.6418 \\ 71.7527 \mp j162.1314 & -190.1986 \mp j341.8549 \end{bmatrix}$
$P(J)$: 0	$\begin{bmatrix} R_{dd}(J) & R_{dq}(J) \\ R_{qd}(J) & R_{qq}(J) \end{bmatrix}$: $\begin{bmatrix} -10.626 & 0 \\ -139.1280 & 0 \end{bmatrix}$

Note: $P(\cdot)$ denotes the poles operator. $R_{dd}(\cdot)$, $R_{dq}(\cdot)$, $R_{qd}(\cdot)$, and $R_{qq}(\cdot)$ denote the *dd*-, *dq*-, *qd*-, and *qq*-axis residues operators, respectively.

1) SELECTIVE IDENTIFICATION OF THE CURRENT CONTROL-RELATED MODE

The sensitivity indexes of the 19 partial fraction terms when the fitting frequency interval is [1, 25] Hz are listed in the second and third columns in Table 8. It can be observed that $A_{1,2}$, $C_{1,2}$, $B_{1,2}$, and $I_{1,2}$ have the largest, second largest, third largest, and fourth largest sensitivity indexes, respectively, which indicates that they are the most, second most, third most, and fourth most likely to be identified from the BLFRs within [1, 25] Hz. Fig. 13(a) plots the poles distribution of the VSC AFRs and the fitted 4th-, 8th-, and 10th-order rational function approximations (i.e., $Y_{vc\_vsc\_4th}^{[1,25]}$, $Y_{vc\_vsc\_8th}^{[1,25]}$, and $Y_{vc\_vsc\_10th}^{[1,25]}$). It can be seen that $Y_{vc\_vsc\_4th}^{[1,25]}$ can only capture $P(A_{1,2})$. However, $Y_{vc\_vsc\_8th}^{[1,25]}$ can capture $P(A_{1,2})$, $P(C_{1,2})$, and $P(B_{1,2})$. $Y_{vc\_vsc\_10th}^{[1,25]}$ can capture $P(A_{1,2})$, $P(C_{1,2})$, $P(B_{1,2})$, and $P(I_{1,2})$ with high precision. The practical fitting results shown in Fig. 13(a) agree with the sensitivity index-based fitting behavior prediction shown in Table 8 which verifies the effectiveness of the derived sensitivity index.

TABLE 8. **Sensitivity Indexes of the Partial Fraction Terms of $Y_{vc\_vsc}^{qq}(s)$ When the AFRs within [1, 25] Hz and [26, 50] Hz are Fitted.**

Term i	$\omega_l = 2\pi1$ rad/s, $\omega_u = 2\pi25$ rad/s		$\omega_l = 2\pi26$ rad/s, $\omega_u = 2\pi50$ rad/s	
	$\lvert\zeta'_P(P(i), R_{qq}(i))\rvert$	$\lvert\zeta'_R(P(i), R_{qq}(i))\rvert$	$\lvert\zeta'_P(P(i), R_{qq}(i))\rvert$	$\lvert\zeta'_R(P(i), R_{qq}(i))\rvert$
$A_{1,2}$	3.8729	0.2722	7.2974	0.5894
$B_{1,2}$	0.0020	0.0053	0.0019	0.0043
$C_{1,2}$	0.0110	0.0144	4.9948×10^{-6}	1.5033×10^{-4}
$D_{1,2}$	2.8275×10^{-7}	6.7881×10^{-6}	3.0502×10^{-7}	7.1423×10^{-6}
$E_{1,2}$	2.4812×10^{-7}	6.2165×10^{-6}	2.6678×10^{-7}	6.5263×10^{-6}
$F_{1,2}$	4.3417×10^{-9}	7.1839×10^{-7}	4.5119×10^{-9}	7.3704×10^{-7}
$G_{1,2}$	1.4019×10^{-10}	1.2849×10^{-7}	1.4521×10^{-10}	1.3154×10^{-7}
H_1	2.7226×10^{-8}	1.8736×10^{-6}	2.7226×10^{-8}	1.8732×10^{-6}
H_2	1.4094×10^{-9}	4.6748×10^{-7}	1.4094×10^{-9}	4.6734×10^{-7}
$I_{1,2}$	1.9612×10^{-4}	5.8622×10^{-4}	9.5210	0.9206
J	1.0484×10^{-8}	1.1459×10^{-6}	9.1778×10^{-9}	1.0201×10^{-6}

Note: $P(\cdot)$ denotes the poles operator. $R_{qq}(\cdot)$ denote the qq-axis residues operator.

2) SELECTIVE IDENTIFICATION OF THE VOLTAGE CONTROL-RELATED MODE

The sensitivity indexes of the 19 partial fraction terms when the fitting frequency interval is [26, 50] Hz are listed in

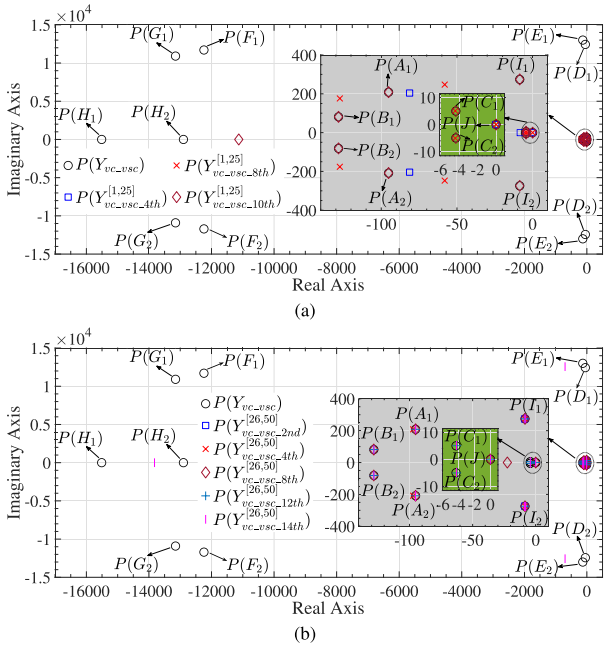

FIGURE 13. Poles distribution of the fitted rational function approximations for the *dq*-domain AFRs of the voltage-controlled VSC within (a) [1, 25] Hz and (b) [26, 50] Hz.

the third and fourth columns in Table 8. It can be observed that $I_{1,2}$, $A_{1,2}$, $B_{1,2}$, $C_{1,2}$, and $D_{1,2}$ have the largest, second largest, third largest, fourth largest, and fifth largest sensitivity indexes, respectively, which indicates that they are the most, second most, third most, fourth most, and fifth most likely to be identified from the BLFRs within [26, 50] Hz. Fig. 13(b) plots the poles distribution of the VSC AFRs and the fitted 2nd-, 4th-, 8th-, 12th-, and 14th-order rational function approximations (i.e., $Y^{[26,50]}_{vc\_vsc\_2nd}$, $Y^{[26,50]}_{vc\_vsc\_4th}$, $Y^{[26,50]}_{vc\_vsc\_8th}$, $Y^{[26,50]}_{vc\_vsc\_12th}$, and $Y^{[26,50]}_{vc\_vsc\_14th}$). It can be seen that $Y^{[26,50]}_{vc\_vsc\_2nd}$ can only capture $P(I_{1,2})$. However, $Y^{[26,50]}_{vc\_vsc\_4th}$ can capture $P(I_{1,2})$ and $P(A_{1,2})$. $Y^{[26,50]}_{vc\_vsc\_8th}$ can capture $P(I_{1,2})$, $P(A_{1,2})$, and $P(B_{1,2})$. $Y^{[26,50]}_{vc\_vsc\_12th}$ can capture $P(I_{1,2})$, $P(A_{1,2})$, $P(B_{1,2})$, and $P(C_{1,2})$. $Y^{[26,50]}_{vc\_vsc\_14th}$ can capture $P(I_{1,2})$, $P(A_{1,2})$, $P(B_{1,2})$, $P(C_{1,2})$, and $P(D_{1,2})$. The practical fitting results shown in Fig. 13(b) agree with the sensitivity index-based fitting behavior prediction shown in Table 8 which verifies the effectiveness of the derived sensitivity index.

VI. CONCLUSION

This article explores and further develops the extrapolation capability of the VF/MF algorithm to identify the out-of-band critical dynamics from the band-limited impedance/admittance data. The proposed extrapolation method extracts the useful information from the band-limited frequency responses to a large extent. This superior extrapolation capability is especially useful if the imaginary parts of the modes of interest are not located in the available frequency range of the impedance/admittance frequency responses, which may contribute to the black box-based state-space modeling and further eigenvalue-based stability analysis. The effects of the practical measurement noise on the extrapolation capability should also be investigated in future. Furthermore, whether the proposed sensitivity index and the corresponding extrapolation capability are applicable for other least-squares-based curve fitting algorithms should be further investigated.

APPENDIX. CIRCUIT AND CONTROLLER PARAMETERS OF THE VSC

The per-unit circuit and controller parameters of the grid-following VSC in Fig. 3 are listed in Table 9, where the base power, base voltage, and base frequency are selected as 2.0 MVar, 575 V, and 50 Hz, respectively.

TABLE 9. Circuit and Controller Parameters of the VSC.

Parameter	Value
DC-link voltage V_{dc}	2 p.u.
Grid phase-to-phase Vrms V_g	1 p.u.
Grid fundamental frequency f_1	1 p.u.
Sampling frequency f_s	100 p.u.
Switching frequency f_{sw}	50 p.u.
Converter-side filter resistance R_{f1}	6.049×10^{-3} p.u.
Converter-side filter inductance L_{f1}	0.475 p.u.
Grid-side filter resistance R_{f2}	6.049×10^{-3} p.u.
Grid-side filter inductance L_{f2}	0.475 p.u.
Filter capacitance C_f	2.597×10^{-3} p.u.
Proportional gain of dc-link voltage controller K_{pvdc}	12.197 p.u.
Integral gain of dc-link voltage controller K_{ivdc}	48.79 p.u.
Proportional gain of PCC voltage controller K_{pvpcc}	0.115 p.u.
Integral gain of PCC voltage controller K_{ivpcc}	0.46 p.u.
Proportional gain of current controller K_{pi}	1.052×10^{-3} p.u.
Integral gain of current controller K_{ii}	4.22×10^{-3} p.u.
Proportional gain of PLL K_{ppll}	0.039 p.u.
Integral gain of PLL K_{ipll}	3.9×10^{-3} p.u.
Active current reference i^{ref}_{2d}	0.498 p.u.
Reactive current reference i^{ref}_{2q}	0 p.u.

REFERENCES

[1] B. Kroposki et al., "Achieving a 100% renewable grid: Operating electric power systems with extremely high levels of variable renewable energy," *IEEE Power Energy Mag.*, vol. 15, no. 2, pp. 61–73, Mar. 2017.

[2] A. Khan, M. Hosseinzadehtaher, M. B. Shadmand, S. Bayhan, and H. Abu-Rub, "On the stability of the power electronics-dominated grid: A new energy paradigm," *IEEE Ind. Electron. Mag.*, vol. 14, no. 4, pp. 65–78, Dec. 2020.

[3] N. Hatziargyriou et al., "Definition and classification of power system stability-revisited & extended," *IEEE Trans. Power Syst.*, vol. 36, no. 4, pp. 3271–3281, Jul. 2021.

[4] J. Beerten, S. D'Arco, and J. A. Suul, "Identification and small-signal analysis of interaction modes in VSC MTDC systems," *IEEE Trans. Power Del.*, vol. 31, no. 2, pp. 888–897, Apr. 2016.

[5] S. D'Arco, J. A. Suul, and J. Beerten, "Configuration and model order selection of frequency-dependent π models for representing DC cables in small-signal eigenvalue analysis of HVDC transmission systems," *IEEE J. Emerg. Sel. Topics Power Electron.*, vol. 9, no. 2, pp. 2410–2426, Apr. 2021.

[6] W. Zhou, R. E. Torres-Olguin, Y. Wang, and Z. Chen, "A gray-box hierarchical oscillatory instability source identification method of multiple-inverter-fed power systems," *IEEE J. Emerg. Sel. Topics Power Electron.*, vol. 9, no. 3, pp. 3095–3113, Jun. 2021.

[7] W. Zhou et al., "A robust circuit and controller parameters' identification method of grid-connected voltage-source converters using vector fitting algorithm," *IEEE J. Emerg. Sel. Topics Power Electron.*, vol. 10, no. 3, pp. 2748–2763, Jun. 2022.

[8] M. K. Bakhshizadeh et al., "The application of vector fitting to eigenvalue-based harmonic stability analysis," *IEEE J. Emerg. Sel. Topics Power Electron.*, vol. 5, no. 4, pp. 1487–1498, Dec. 2017.

[9] A. Rygg and M. Molinas, "Apparent impedance analysis: A small-signal method for stability analysis of power electronic-based systems," *IEEE J. Emerg. Sel. Topics Power Electron.*, vol. 5, no. 4, pp. 1474–1486, Dec. 2017.

[10] Y. Wang, X. Wu, Z. Li, X. Xiao, X. Xie, and Y. Wang, "Vector-fitting-based quantitative SSCI analysis for series-compensated wind power systems," *IET Renew. Power Gener.*, vol. 14, no. 15, pp. 3023–3034, Nov. 2020.

[11] M. Zhang, Z. Miao, L. Fan, and S. Shah, "Data-driven interarea oscillation analysis for a 100% IBR-penetrated power grid," *IEEE Open Access J. Power Energy*, vol. 10, pp. 93–103, 2023.

[12] B. Gustavsen and A. Semlyen, "Rational approximation of frequency domain responses by vector fitting," *IEEE Trans. Power Del.*, vol. 14, no. 3, pp. 1052–1061, Jul. 1999.

[13] Y. Hu, W. Wu, A. M. Gole, and B. Zhang, "A guaranteed and efficient method to enforce passivity of frequency-dependent network equivalents," *IEEE Trans. Power Syst.*, vol. 32, no. 3, pp. 2455–2463, May 2017.

[14] J. M. Rodriguez, E. Medina, J. Mahseredjian, A. Ramirez, K. Sheshyekani, and I. Kocar, "Frequency-domain fitting techniques: A review," *IEEE Trans. Power Del.*, vol. 35, no. 3, pp. 1102–1110, Jun. 2020.

[15] J. Beerten, S. D'Arco, and J. A. Suul, "Frequency-dependent cable modelling for small-signal stability analysis of VSC-HVDC systems," *IET Gener., Transmiss. Distrib.*, vol. 10, no. 6, pp. 1370–1381, Apr. 2016.

[16] C. A. Ruiz-Zea et al., "Dual-band reduced-order model of an HVDC link embedded into a power network for EMT studies," *IEEE Trans. Energy Convers.*, vol. 35, no. 1, pp. 416–424, Mar. 2020.

[17] B. Gustavsen, "Improving the pole relocating properties of vector fitting," *IEEE Trans. Power Del.*, vol. 21, no. 3, pp. 1587–1592, Jul. 2006.

[18] T. Noda, "Identification of a multiphase network equivalent for electromagnetic transient calculations using partitioned frequency response," *IEEE Trans. Power Del.*, vol. 20, no. 2, pp. 1134–1142, Apr. 2005.

[19] A. Ramirez, "Vector fitting-based calculation of frequency-dependent network equivalents by frequency partitioning and model-order reduction," *IEEE Trans. Power Del.*, vol. 24, no. 1, pp. 410–415, Jan. 2009.

[20] A. Ramirez and R. Iravani, "Enhanced fitting to obtain an accurate DC response of transmission lines in the analysis of electromagnetic transients," *IEEE Trans. Power Del.*, vol. 29, no. 6, pp. 2614–2621, Dec. 2014.

[21] M. Cervantes, I. Kocar, J. Mahseredjian, and A. Ramirez, "Partitioned fitting and DC correction for the simulation of electromagnetic transients in transmission lines/cables," *IEEE Trans. Power Del.*, vol. 33, no. 6, pp. 3246–3248, Dec. 2018.

[22] B. Gustavsen, "Fast passivity enforcement for pole-residue models by perturbation of residue matrix eigenvalues," *IEEE Trans. Power Del.*, vol. 23, no. 4, pp. 2278–2285, Oct. 2008.

[23] J. Morales, J. Mahseredjian, K. Sheshyekani, A. Ramirez, E. Medina, and I. Kocar, "Pole-selective residue perturbation technique for passivity enforcement of FDNEs," *IEEE Trans. Power Del.*, vol. 33, no. 6, pp. 2746–2754, Dec. 2018.

[24] E. Medina, A. Ramirez, J. Morales, and J. Mahseredjian, "Alternative approach to alleviate passivity violations of rational-based fitted functions," *IEEE Trans. Power Del.*, vol. 34, no. 3, pp. 1161–1170, Jun. 2019.

[25] S. Grivet-Talocia and M. Bandinu, "Improving the convergence of vector fitting for equivalent circuit extraction from noisy frequency responses," *IEEE Trans. Electromagn. Compat.*, vol. 48, no. 1, pp. 104–120, Feb. 2006.

[26] J. Becerra, F. Vega, and F. Rachidi, "Extrapolation of a truncated spectrum with Hilbert transform for obtaining causal impulse responses," *IEEE Trans. Electromagn. Compat.*, vol. 59, no. 2, pp. 454–460, Apr. 2017.

[27] J. Cho, K. Hwang, S. Jeung, and S. Ahn, "An efficient extrapolation method of band-limited S-parameters for extracting causal impulse responses," *IEEE Trans. Comput.-Aided Design Integr. Circuits Syst.*, vol. 38, no. 11, pp. 2086–2098, Nov. 2019.

[28] J. Cho et al., "Low- and high-frequency extrapolation of band-limited frequency responses to extract delay causal time responses," *IEEE Trans. Electromagn. Compat.*, vol. 63, no. 3, pp. 888–901, Jun. 2021.

[29] M. H. Richardson and D. L. Formenti, "Parameter estimation from frequency response measurements using rational fraction polynomials," in *Proc. 1st Int. Modal Anal. Conf.*, Orlando, FL, USA, 1982, pp. 167–181.

[30] M. H. Richardson, "Global frequency & damping estimates from frequency response measurements," in *Proc. 4st Int. Modal Anal. Conf.*, Los Angeles, CA, USA, 1986, pp. 465–470.

[31] D. Formenti and M. Richardson, "Parameter estimation from frequency response measurements using rational fraction polynomials (twenty years of progress)," in *Proc. 20th Int. Modal Anal. Conf.*, Los Angeles, CA, USA, 2002, pp. 373–382.

[32] W. Zhou, R. E. Torres-Olguin, Y. Wang, and Z. Chen, "DQ impedance-decoupled network model-based stability analysis of offshore wind power plant under weak grid conditions," *IET Power Electron.*, vol. 13, no. 13, pp. 2715–2729, Oct. 2020.

[33] J. Huang, K. A. Corzine, and M. Belkhayat, "Small-signal impedance measurement of power-electronics-based AC power systems using line-to-line current injection," *IEEE Trans. Power Electron.*, vol. 24, no. 2, pp. 445–455, Feb. 2009.

[34] T. Roinila, T. Messo, and E. Santi, "MIMO-identification techniques for rapid impedance-based stability assessment of three-phase systems in DQ domain," *IEEE Trans. Power Electron.*, vol. 33, no. 5, pp. 4015–4022, May 2018.

[35] W. Zhou and J. Beerten, "Insight into frequency-domain extrapolations of least-squares-based curve fitting algorithms," in *Proc. 47th Annu. Conf. IEEE Ind. Electron. Soc.*, Oct. 2021, pp. 1–6.

[36] W. Zhou and J. Beerten, "Extrapolation of band-limited frequency responses for out-of-band modal synthesis," in *Proc. Int. Power Electron. Conf. (IPEC-Himeji ECCE Asia)*, May 2022, pp. 1578–1583.

WEIHUA ZHOU (Member, IEEE) received the B.Eng. and M.Sc. degrees in electrical engineering from the School of Automation, Northwestern Polytechnical University, Xi'an, China, in 2014 and 2017, respectively, and the Ph.D. degree in electrical engineering from the Department of Energy Technology, Aalborg University, Aalborg, Denmark, in 2020.

From November 2015 to May 2016, he was a Junior Research Assistant with the Department of Mechanical and Automation Engineering, The Chinese University of Hong Kong, Hong Kong. From August 2020 to November 2020, he was a Visiting Scholar with the Department of Marine Technology, Norwegian University of Science and Technology, Trondheim, Norway. In 2021, he was a Research Fellow with the Electa Research Group, Department of Electrical Engineering, KU Leuven, Belgium, and EnergyVille, Genk, Belgium. He is currently a Research Fellow with the Department of Electrical and Computer Systems Engineering, Monash University, Melbourne, Australia. His research interests include modeling, stability analysis, and control of inverter-based resources.

JEF BEERTEN (Senior Member, IEEE) received the M.Sc. and Ph.D. degrees in electrical engineering from the University of Leuven (KU Leuven), Belgium, in 2008 and 2013, respectively.

In 2011, he was a Visiting Researcher with the Royal Institute of Technology (KTH), Stockholm, Sweden, for three months. From April 2014 until March 2015, he was a Visiting Post-Doctoral Researcher with the Norwegian University of Science and Technology (NTNU), Trondheim, Norway. Currently, he is an Associate Professor with KU Leuven and EnergyVille. His research interests include future power system dynamics, modeling, and control.

Dr. Beerten is an Active Member of IEEE and CIGRE. He was the first winner of the ABB Research Award in Honor of Hubertus von Gruenberg in 2016. He received the KBVE/SRBE Robert Sinave Award and the Prix Paul Caseau from the Institut de France-EDF Foundation for his Ph.D. thesis on modeling and control of DC grids.